thesis for the degree of Licentiate of Philosophy in Physics

Computational Investigation of Charge Localization and Structural Dynamics in Halide Perovskites

Mehmet Baskurt

Department of Physics
chalmers university of technology
Göteborg, Sweden 2025

Computational Investigation of Charge Localization
and Structural Dynamics in Halide Perovskites
Mehmet Baskurt

Department of Physics
Chalmers University of Technology
se-412 96 Göteborg, Sweden
Telephone +46 (0)31 772 10 00

Cover: Self-trapped exciton isosurface in $Cs_2AgBiBr_6$ halide double perovskite.

Chalmers digitaltryck
Göteborg, Sweden 2025

Computational Investigation of Charge Localization and Structural Dynamics in Halide Perovskites

Mehmet Baskurt
Department of Physics
Chalmers University of Technology

Abstract

Halide perovskites have gained significant interest due to their remarkable optoelectronic properties and diverse applications. However, most of these applications involve lead-based halide perovskites which suffer from critical challenges related to lead toxicity and long-term stability. In order to counter these challenges various strategies have been explored, including encapsulation, surface passivation, compositional engineering, and alternative synthesis techniques. One of the promising approaches is the development of lead-free halide perovskites. In this licentiate thesis, a computational study is conducted on these materials, using advanced Density Functional Theory calculations and Molecular Dynamics simulations employing neuroevolution potentials. The structural properties, with a particular focus on octahedral tilting and phase transitions are explored. Furthermore, charge localizations in the form of polarons in $Cs_2AgBiBr_6$ and $CsGeX_3$ (X=Cl,Br,I) are investigated. Additionally, the formation of self-trapped excitons in $Cs_2AgBiBr_6$ is examined. These self-trapped states play an important role in the material optical properties reported in several experimental reports. Overall, the results in this work provide valuable insights on the structural and electronic properties of lead-free halide perovskites.

Keywords: density functional theory, molecular dynamics, lead-free, halide perovskites, halide double perovskite, polaron, self-trapped exciton

LIST OF APPENDED PAPERS

I **Charge Localization in $Cs_2AgBiBr_6$ Double Perovskite: Small Polarons and Self-Trapped Excitons**
M. Baskurt, J. Wiktor
The Journal of Physical Chemistry C 127, 49, 23966–23972 (2023)
doi: 10.1021/acs.jpcc.3c06551

II **Effects of Lone-Pair Electrons on the Octahedral Tilting in Halide Double Perovskites**
M. Baskurt, M. Karlsson, E. Fransson, P. Erhart J. Wiktor
In manuscript

III **Exploring the Polaron Landscape in Lead-Free Germanium Halide Perovskites: $CsGeCl_3$, $CsGeBr_3$, and $CsGeI_3$**
M. Baskurt, J. Wiktor
In manuscript

The author's contribution to the papers:

I The author carried out the calculations and analysis, prepared the figures and wrote the paper.

II The author carried out most of the density functional theory calculations and analysis. The author trained neuroevolution potentials and performed molecular dynamics simulations and analysis, prepared the figures and wrote the paper.

III The author performed the calculations and analysis, prepared the figures and wrote the paper.

PUBLICATIONS NOT INCLUDED IN THIS THESIS

Direct, Indirect, and Self-Trapped Excitons in $Cs_2AgBiBr_6$
M. Baskurt, P. Erhart, J. Wiktor
The Journal of Physical Chemistry Letters 15, 33, 8549–8554 (2024)

Contents

List of abbreviations

AIMD *ab initio* Molecular Dynamics. 26

ANN artificial neural network. 27

CBM conduction band minimum. 4, 15, 16, 25

DFT Density Functional Theory. vii, 2, 19, 21–23, 26, 28, 31, 33, 35

GHP Germanium halide perovskite. 3, 15, 16, 33

HDP Halide Double Perovskite. 2–6, 9–11, 18, 26, 32, 35, 36

HF Hartree-Fock. 20, 21, 24, 31

MD Molecular Dynamics. 2, 10, 25, 26, 28, 29, 32, 35

NEP Neuroevolution Potential. 27–29, 35

PL photoluminescence. 5, 15, 17, 31, 32

STE self-trapped exciton. 2, 15–18, 31, 32, 35, 36

VBM valence band maximum. 15, 16, 25

1

Introduction

In 1839, a mineral was discovered in the Ural Mountains extending across western Russia by Gustav Rose. This mineral was $CaTiO_3$, and its crystals showed a clear cubic structure. This mineral was named after the Russian mineralogist Lev Perovski. Later on, the name 'perovskite' was applied to the class of materials with the general chemical formula ABX_3 that exhibit the same type of arrangement of atoms. In the mid-20th century, perovskites gained significant interest. Numerous perovskite oxides were explored and their interesting properties such as ferroelectricity, piezoelectricity, catalytic activity, and ionic conductivity were revealed. In the early 2000s, synthetic perovskites containing halogens, namely metal halide perovskites, rose to the scene [1]. In a remarkably short period, metal halide perovskites have captivated researchers with their extraordinary properties and found their way into solar cells, light-emitting diodes and sensor technologies [2, 3].

The phenomenal performance, coupled with relatively sustainable and low-cost fabrication methods, positions metal halide perovskites at the forefront of emerging solar technologies to replace traditional Si-based devices. The power conversion efficiency (PCE) of perovskite-based solar cells tremendously improved in less than two decades, surpassing 24% [4]. Moreover, their combination with silicon-based solar cells has achieved PCE of 33.9% [5]. This joint configuration, namely silicon-perovskite tandem solar cells, captures sunlight across different regions of the solar spectrum, resulting in more efficient power conversion. Beyond exceptional performance, perovskite solar cells offer low-cost and scalable fabrication [6, 7].

Band gap tunability through compositional engineering and scalable fabrication also make metal halide perovskites an attractive group of materials for light-emitting diodes (LEDs) [8], for example, in high-quality backlit displays of perovskite@glass composites [9]. This backlit display is reported to cover a wide color gamut of 176% of commercial LCDs and 127% of the NTSC 1953 standard, there-

fore achieving high color-accuracy. Moreover, through solution processing, the production cost of perovskite-based LEDs can be lowered further by employing methods such as inkjet printing [10].

The fast response time and high sensitivity make halide perovskite crystals great candidates in sensor applications [11]. It is reported that perovskite-based sensors can even be used to mimic all five human senses such as vision, olfaction, tactility, palate, and hearing [12]. Thus, halide perovskite based sensors can be utilized in future applications of medical equipment and bionic prosthetics.

Although halide perovskites are promising materials for high-performance optoelectronic device applications, they face significant challenges, such as stability and toxicity issues. It is worth noting that the most effective and widely used halide perovskites are generally lead-based. Lead (Pb), a neurotoxin that can have serious detrimental effects on human health, limits the widespread use of lead-based metal halide perovskites [13, 14]. Furthermore, lead-based halide perovskites tend to degrade over time under environmental conditions. This can lead to contamination of soil and water, posing a serious environmental threat. In addition to the health concerns, degradation under environmental conditions is a vulnerability to their long-term performance [15, 16]. To overcome such drawbacks, researchers have explored various approaches. One strategy involves reducing lead leakage from lead-halide solar modules through different encapsulation methods [17]. Another approach focuses on developing lead-free alternatives of perovskite crystals that exhibit properties similar to those of lead-based counterparts [18]. In this thesis, I explore the properties of lead-free halide perovskites using Density Functional Theory and Molecular Dynamics simulations.

The primary objective of this thesis is to investigate the structural dynamics and charge localizations inherent in lead-free halide perovskites. I examine the various structural phases of halide double perovskites and phase transitions caused by temperature changes. These transitions are characterized by octahedral tilting and I discuss the contribution of different factors that play a role in this process. Finally, through hybrid density functional theory modeling, I study polarons and self-trapped excitons in lead-free halide perovskites such as $Cs_2AgBiBr_6$ and $CsGeX_3$ (X = Cl, Br, I).

The remainder of this thesis is organized as follows. In Chapter 2, a brief overview of lead-free halide perovskites is provided. Lead-free Halide Double Perovskite, their crystal structure, the effects of different compositions, and their applications are discussed. In Chapter 3, the mechanics of phase transitions is explained. In Chapter 4, I cover the charge localization in halide perovskites as well as its impact and related challenges in modeling. In Chapter 5, the computational methods used in this thesis are introduced. Chapter 6 summarizes the three papers that make the basis of this thesis. Finally, the thesis is concluded and a brief outlook is provided in Chapter 7.

2

Lead-Free Halide Perovskites

As discussed in Chapter 1, although lead-based halide perovskites exhibit remarkable optoelectronic properties, due to health and environmental concerns, considerable attention in the perovskite community has shifted toward exploring lead-free alternatives. For example, the substitution of Pb with other 4A group elements of the periodic table such as tin (Sn) or germanium (Ge) could be expected to remove toxicity while keeping the exceptional performance. Thanks to their ideal band gap [19], exceptionally long carrier lifetime [20], and high charge carrier mobility [21], tin halide perovskites were hoped to resolve the limitations of their lead-based counterparts. Unfortunately, they have displayed performance inferior to those of the Pb-based perovskites in a range of applications. Moreover, the strong tendency of Sn^{2+} to oxidize to Sn^{4+} in Sn-based halide perovskites leads to unwanted p-type doping and increases charge carrier populations, which significantly alters the electronic properties of the host material [22–25]. Ge-based halide perovskites, like their Sn-based counterparts, are prone to oxidation but are generally considered more stable. Although their PCE is inferior even compared to Sn-based perovskite solar cells [26, 27], due to their high structural stability and non-toxic nature, they are still considered candidates for photovoltaics [28]. Moreover, Germanium halide perovskite (GHP)s are reported to be promising materials in non-linear optics [29].

Ge-based perovskites show an important distinction in terms of their crystal structure. Unlike Pb- and Sn-based perovskites, Ge-based perovskites do not exhibit a high degree of octahedral tilting. Instead, at low temperatures, the Ge cation in the GeX_6 octahedron becomes off-centered, leading to a low-symmetry rhombohedral or monoclinic structure [29, 30]. As will be shown in Chapter 4, this cation off-centering can have a significant impact, for example on the polaron formation.

Alternatively, another group has emerged as lead-free analogs, Halide Double

Perovskites [31]. A major part of this thesis is focused on the members of this material group.

2.1 Halide Double Perovskites

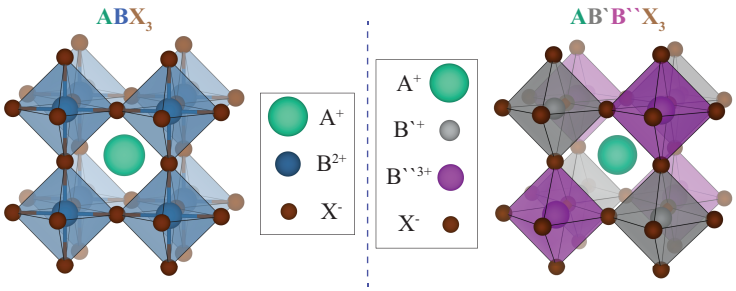

Figure 2.1: Crystal structure of single (left) and double (right) perovskites.

Halide Double Perovskite (HDP)s are the product of substituting the divalent Pb^{2+} ion with two distinct group elements, monovalent B^{i+} and trivalent $B^{ii\ 3+}$, resulting in a formula of $AB^iB^{ii}X_6$. The crystal structure of HDPs consists of B^+X_6 and $B^{3+}X_6$ octahedra in alternating arrangement where X is a halogen atom, and A is a monovalent cation such as Cs^+ or Rb^+, as presented in Fig. 2.1. Increased degrees of freedom in the selection of B-cations allow for tailoring their electronic properties further for specific applications [32]. For example, in Fig. 2.2 electronic band structures of $Cs_2AgBiBr_6$, Cs_2AgBiI_6, $Cs_2AgSbBr_6$, $Cs_2AgSbBr_6$, $Cs_2TlBiCl_6$, and $Cs_2TlBiBr_6$ Halide Double Perovskite (HDP)s are presented. It is observed that a Halide Double Perovskite (HDP) containing Tl and Bi results in a relatively large direct band gap at Γ, while replacing Tl with Ag reduces the band gap and shifts the CBM to the R point. Additionally, halogen substitution increases the band gap in the order I → Br → Cl. The compositional variety offers a high number of possible HDP configurations. Up until now, over 900 possible HDPs have been identified. Among these, 350 have been successfully synthesized, meanwhile, over 600 compounds remain to be investigated [33].

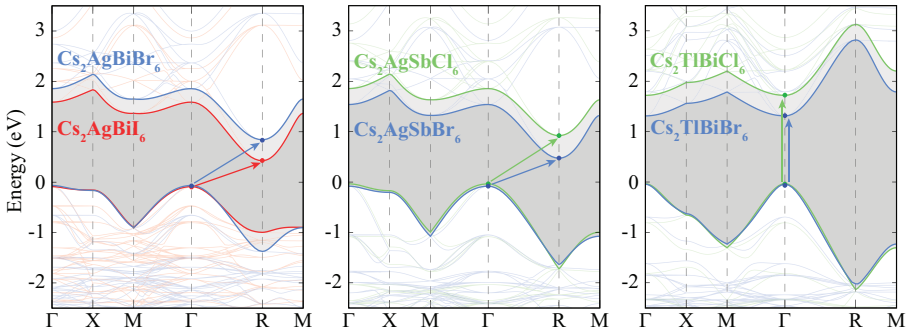

Figure 2.2: Electronic band structures of halide double perovskites $Cs_2AgBiBr_6$, $Cs_2AgSbBr_6$, $Cs_2AgInCl_6$ calculated with PBE functional.

Halide Double Perovskite (HDP)s find diverse applications, including solar cells [34, 35], LEDs [36], photocatalysts [37], photodetectors [38, 39], and X-ray detectors [40]. Based on their composition, HDPs can be categorized as Bi-based, Sb-based, In-based, Fe-based, Tl-based and Au-based [41]. Bi-based HDPs are considered one of the most promising groups for photovoltaics, due to their electronic configuration that allows high light absorption and long carrier lifetimes [18, 42, 43]. The star of its class, $Cs_2AgBiBr_6$, displays remarkable moisture resistance and thermal stability, yielding up to 240 days of stability in ambient atmosphere [44]. It exhibits high absorption below 3.6 eV (340 nm), a strong feature around 2.8 eV (440 nm), and weak absorption around 1.9 eV (650 nm), expected to arise from an indirect bandgap [45]. In addition to absorption, a photoluminescence (PL) signal has been observed at 1.95 eV, however, its origin has not been fully understood up to now [46]. The unresolved question related to the PL peak motivated the computational analysis in **Paper I**. Our results show that experimentally reported emission properties of $Cs_2AgBiBr_6$ mainly arise from self-trapped states, and it is further discussed in Chapter 4.

Sb-based HDPs, similar to the Bi-based ones, are also broadly researched for their use in photovoltaics [47]. For example, $Cs_2AgSbBr_6$ is one of the most studied Sb-based HDPs. It resembles $Cs_2AgBiBr_6$ and crystallizes in the cubic phase, with the space group $Fm\bar{3}m$. However, the synthesis of this HDP yields significant amounts of secondary phases such as $Cs_3Sb_2Br_9$ and Cs_2SbBr_6. The existence of these secondary phases reduces light absorption and charge carrier transport, thus lowering the device efficiency. $Cs_2AgSbBr_6$ exhibit an indirect band gap with a shallow absorption edge at 1.64 eV [47].

In-based HDPs such as $Cs_2AgInCl_6$ gained vast interest owing to their direct band gap and ambient stability [48]. Strong optical absorption below 300 nm and weak absorption around 378 nm are experimentally reported for bulk $Cs_2AgInCl_6$. Moreover, this HDP exhibits a broad PL peak around 600 nm. However, its lower photoluminescence quantum yield and worse tolerance to ambient conditions make

the competition against lead-based halide perovskites challenging for this material.

Due to their soft nature, HDPs can undergo transitions between different phases such as cubic, tetragonal, or orthorhombic. Such structural phase transitions occur as a function of temperature due to a relatively small A-cation that brings about octahedral tilting instabilities [49]. The collapse of soft phonon branches can lead to phase transitions [50]. Phase transitions can affect for example stability, transport, and optoelectronic properties of halide perovskites. Therefore, exploring underlying factors like tilting instabilities that influence phase transitions is important for improving the accuracy and efficiency of the computational simulations. The next chapter will focus on the phase stability and transitions in relation to octahedral tilting in halide perovskites.

3

Phase Stability and Transitions in Lead-Free Halide Perovskites

To model a material accurately, one needs to know which phase is relevant at a given temperature. Therefore, this chapter examines phase stability and transitions in lead-free halide perovskites, highlighting the methods used for their characterization and discussing the fundamental driving forces behind these transitions as well as the factors that constrain their stability.

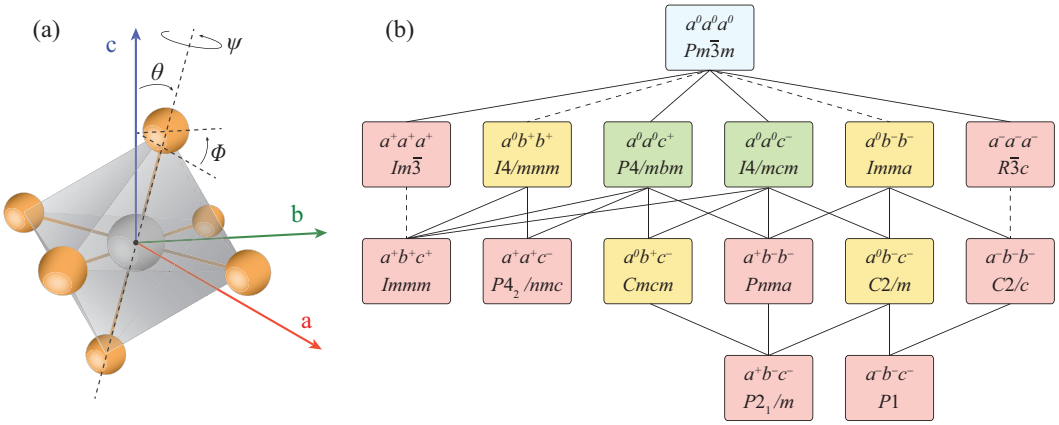

Figure 3.1: (a) Schematic representation of the Euler angles ϕ, θ, and ψ that describe the orientation of the octahedron. (b) Group-subgroup relationships of the tilt systems and space-groups given in Table 3.1. Zero, one, two, and three tilt rotations are indicated by blue, green, yellow, and red colored boxes, respectively. Dashed lines indicate that the corresponding phase transition must be first-order.

A large number of halide perovskites cannot maintain their simple cubic phase

with space group $Pm\bar{3}m$ at room temperature, exhibiting lattice distortions due to the highly flexible framework of corner-sharing [BX_6] octahedra and A cations [51, 52]. The Goldschmidt tolerance factor (t) [49, 53] is an empirical approach to quantifying the size match between A and B-cations in halide perovskites within the cubic phase, and is defined as:

$$t = \frac{r_A + r_X}{\sqrt{2}(r_B + r_X)}, \tag{3.1}$$

where r_A, r_B, and r_X are the radii of A-cation, B-cation, and halogen, respectively. Crystals with a tolerance factor in the range of $0.75 \leq t \leq 1.00$ are more likely to form perovskite structure. Outside of this range, the material is more likely to adopt a different crystal structure. At the lower end of t, where t approaches 0.75, the mismatch between cation sizes leads to distortions like octahedral tilting [52]. The magnitude of these distortions can be described by three Euler angles: ϕ, θ, and ψ (see in Fig. 3.1(a)). Euler angles play an important role in the classification of perovskites. A simple notation that was suggested by Glazer [54] for describing and classifying octahedral tilting in perovskites revealed 23 possible tilt systems. Later on, Howard *et al.* reduced the number of possible structures to 15 by applying group-theoretical methods [51]. Glazer's notation provides a clear and simple way to describe tilting patterns. It utilizes a pseudocubic unit cell where a single octahedron is centered as a reference. The rotation of this unit cell is used to describe the tilting systems, as presented in Table 3.1. Each phase is described by three letters with superscripts $a^i b^j a^k$ where a, b, and c represent the relative tilts along the three principal crystallographic axes, meanwhile the superscript 0, $-$, $+$ indicates the tilt direction relative to the ideal cubic structure. For example $a^0a^0a^0$ corresponds to the cubic phase (no tilting on average), and $a^+b^-c^-$ corresponds to in-phase rotation along the crystallographic direction a and out-of-phase rotation along the crystallographic directions b and c, therefore corresponds to an orthorhombic structure. Rotation axes and the tilt direction are also important to indicate the group-subgroup relationships of the tilts. These group-subgroup relationships, which reveal the prerequisites for transitions between two phases, are displayed in Fig. 3.1(b). However, it is important to note that in certain cases the group-subgroup relation does not apply to the specific domains shown in the figure. For example, $a^0b^-b^-$ is not a subgroup of $a^0a^0c^-$, but a subgroup of $a^0b^-a^0$, which is another domain of $a^0a^0c^-$. Moreover, group-subgroup pairs connected via dashed lines in the diagram are required to be first-order by the Landau theory [55].

Tendencies towards octahedral tilting and phase transitions in metal halide perovskites can be different depending on their composition. In halide double perovskites, this tendency can be analyzed further in relation to the selection of B^i and B^{ii} cations. Due to the inclusion of B cations with different electronic characteristics, perovskite crystals with diverse numbers of lone-pair electrons can be

Table 3.1: Classification of tilts in Glazer's notation for perovskite structures. Tilts are categorized by the number of tilts. tilt class and the tilts columns show the specific tilt direction. Space group, and number of distinct tilt configurations.

	tilt class	tilts	tilt number	space group	N
zero-tilt	0 0 0	$(a^0a^0a^0)$	23	$Pn\bar{3}m(\#221)$	1
one-tilt	0 0 $^-$	$(a^0a^0c^-)$	22	$I4/mcm(\#140)$	4
	0 0 +	$(a^0a^0c^+)$	21	$P4/mbm(\#127)$	2
two-tilt	0 $^-$ $^-$	$(a^0b^-b^-)$	20	$Imma(\#74)$	4
		$(a^0b^-c^-)$	19	$C2/m(\#12)$	4
	0 + $^-$	$(a^0b^+c^-)$	17	$Cmcm(\#63)$	8
	0 + +	$(a^0b^+b^+)$	16	$I4/mmm(\#139)$	8
three-tilt	$^-$ $^-$ $^-$	$(a^-a^-a^-)$	14	$R\bar{3}c(\#167)$	6
		$(a^-b^-b^-)$	13	$C2/c(\#15)$	8
		$(a^-b^-c^-)$	12	$P1(\#2)$	8
	+ $^-$ $^-$	$(a^+b^-b^-)$	10	$Pnma(\#62)$	4
		$(a^+b^-c^-)$	8	$P2_1/m(\#11)$	8
	+ + $^-$	$(a^+a^+c^-)$	5	$P4_1/nmc(\#137)$	8
	+ + +	$(a^+a^+a^+)$	3	$Im\bar{3}(\#204)$	8
		$(a^+b^+c^+)$	1	$Immm(\#71)$	8

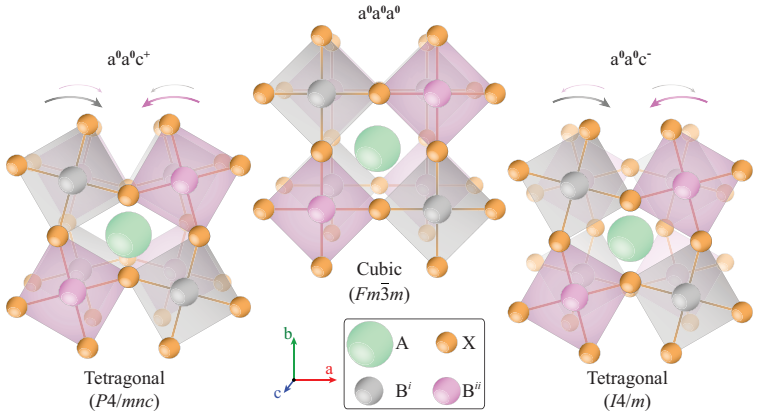

Figure 3.2: Cubic ($Fm\bar{3}m$) and tetragonal ($P4/mnc$ and $I4/m$) phases of halide double perovskite $A_2B^iB^{ii}X_6$ with their corresponding Glazers' notation.

obtained. The effect of the number of lone-pair electrons in metal halide perovskites on the structural dynamics has been previously only examined in specific cases [56]. In **Paper II**, the correlation between the number of lone-pair electrons and octahedral tilting in the broad family of HDPs is further investigated. The relative stabilities of their cubic ($Fm\bar{3}m$) and tetragonal ($P4/mnc$, and $I4/m$) phases are assessed (see Fig. 3.2). Their ground state structures are reported by quantifying

the octahedral tilts after relaxation. I discover a relationship between the number of lone-pair electrons and the degree and stability of tilting in the family of 46 HDPs, where a higher number of lone-pair electrons results in both stronger and more stable octahedral tilting at 0 K. As a consequence, the phase transition temperatures and the degree of local distortions of compounds with a higher number of lone-pairs are generally increased. This insight can be used in designing and engineering double perovskites for specific applications.

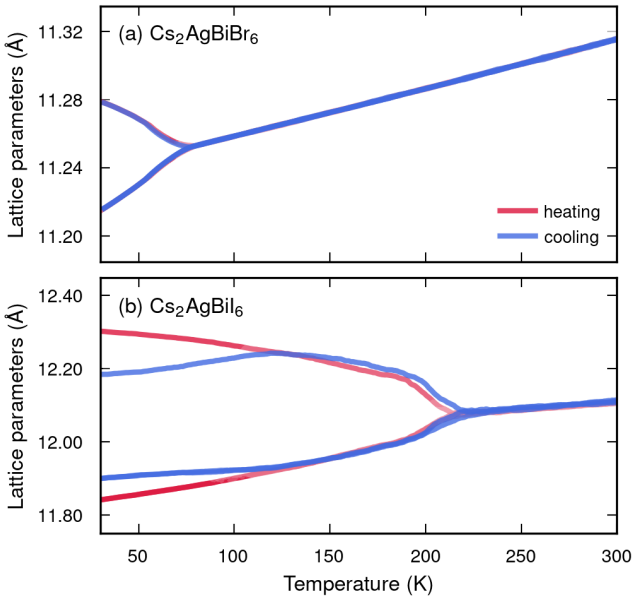

Figure 3.3: Lattice parameters for (a) $Cs_2AgBiBr_6$ and (b) Cs_2AgBiI_6 as a function of temperature from MD simulations. The red and blue lines represent heating and cooling simulations.

Although the number of lone pair electrons has a dominant effect on promoting octahedral tilting, there are additional factors that determine this property. HDPs with single lone pair electron per formula exhibit broad distribution in tilting energies and angles. To better understand the local dynamics of the phase transitions in HDPs, I performed MD simulations using machine-learned potentials for $Cs_2AgBiBr_6$ and Cs_2AgBiI_6. Although these materials have a single stereochemically active lone pair electron per formula unit, substantial differences in their phase dynamics are observed. Fig. 3.3 shows the lattice parameters for $Cs_2AgBiBr_6$ and Cs_2AgBiI_6 as function of temperature. Here, the HDP with energetically less stable (tilting energy of -3.1 meV for $I4/m$, -0.6 meV for $P4/mnc$, per formula unit) and more narrow tilt ($I4/m$: 7.4°, $P4/mnc$: 6.1°), $Cs_2AgBiBr_6$, exhibits a transition from tetragonal to cubic phase around 70 K while Cs_2AgBiI_6 which has tilting energies more favorable by 36.6 meV and 32.0 meV per formula unit for $I4/m$ and

$P4/mnc$, respectively, exhibits two phase transitions at higher temperatures. As presented in Fig. 3.3 (b), Cs_2AgBiI_6 undergoes phase transition from a two-tilt monoclinic phase to a one-tilt tetragonal phase around 120 K, and from tetragonal to cubic phase around 210 K. This implies that tilt energies and angles determined at 0 K can be used as a qualitative indication of the expected phase at finite temperature and the degree of anharmonicity of HDPs.

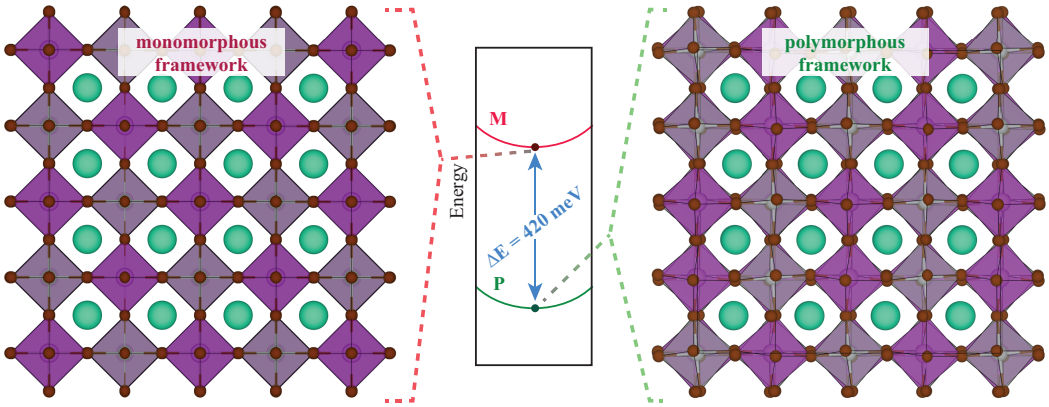

Figure 3.4: Crystal structure of $Cs_2AgBiBr_6$ in monomorphous and polymorphous framework. The inset presents the energy difference between two structural frameworks where the polymorphous structure is 420 meV more favorable than the monomorphous structure.

The existence of multiple perovskite phases also affects the computational modeling. Electronic structure calculations are often done at 0 K in an average structure representing the phase that can sometimes only be stable at finite temperatures. In the context of perovskites, it has been established that perfectly cubic supercells do not represent well for example the electronic structure of the material at finite temperatures [57, 58]. This is because these perfect structures of perovskites used in many simulations fail to capture the complexity of the material's local atomic environment. To address this, rather than assuming a single repeated structural motif (referred to as a *monomorphous structure*), it is more realistic to consider a more complex structure in which multiple lower-symmetry motifs coexist. This distribution of low-symmetry local motifs including octahedral tilting, bond-length variations, and atomic displacements is called a *polymorphous network* [58]. A polymorphous structure has a larger-than-minimal cell size to allow low-symmetry distortions to appear. Zhao *et al.* showed that as the size of the supercell increases, the system's energy decreases compared to the monomorphous cell, stabilizing after 32 formula units. Fig. 3.4 displays an example of the monomorphous and polymorphous crystal structure of $Cs_2AgBiBr_6$, each containing a unit cell with 32 formula units (320 atoms), where the polymorphous structure is energetically

more favorable by 420 meV. The use of polymorphous structures leads to more accurate predictions of electronic properties and better aligns with experimental measurements.

4

Localized Charges in Halide Perovskites

Upon excitation, for example by light or an electrical pulse, an electron-hole pair can be created in a material. Right after excitation, the charges are often assumed to occupy the delocalized valence and conduction states. However, due to interactions with phonons or imperfections, they can become localized. Localized charges in halide perovskites play a pivotal role in the electronic and optical properties of the material and therefore directly impact their performance in optoelectronic applications. Localization can occur as self-trapping (polarons) or in the presence of defects. Defects are imperfections in the crystal structure of the materials and can be intrinsic or extrinsic. Such defects in halide perovskites can be electronically inert or induce electronic states near the conduction or valence band edge, forming shallow traps that affect the charge carrier effective mobility [59]. In contrast, deep defects can introduce trap states further within the bandgap and can be detrimental to the device efficiency [60]. Halide perovskites are expected to exhibit both types of localization, defect and polaron-related. The latter type is studied in this work.

4.1 Polarons

Polarons are quasiparticles that arise due to the strong coupling of excess charge carriers with ionic vibrations. In a polarizable solid, the injection of an excess charge leads to local ionic displacements, creating a polarization cloud [61, 62]. The formation of electron and hole polarons is illustrated in Fig. 4.1. Polarons are reported to play a key role in physical phenomena such as charge carrier mobility,

reactivity, and photoemission [63, 64]. In addition, polaron formation has been suggested to increase defect tolerance in halide perovskites as a result of reducing carrier scattering caused by defects or phonons [65].

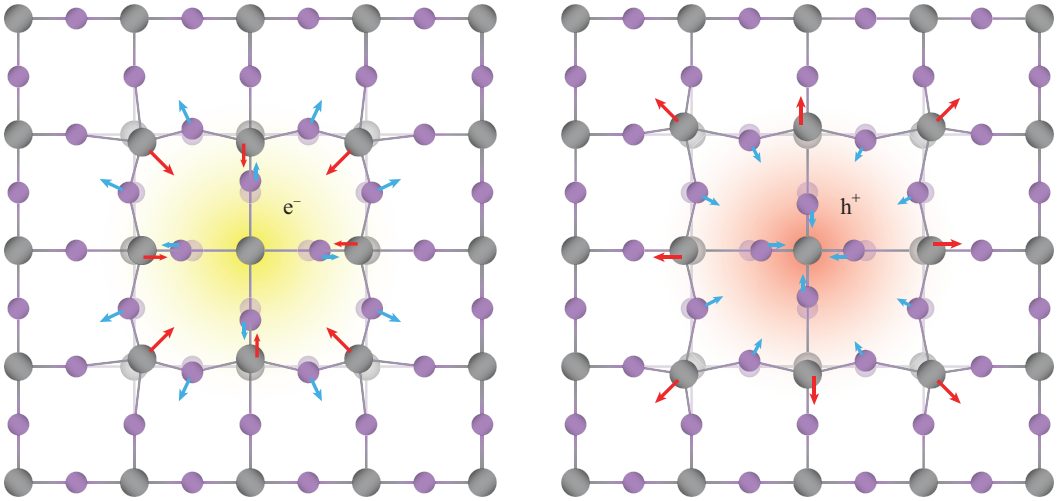

Figure 4.1: Electron and hole polarons

Polarons are classified based on their spatial extent, as small or large polarons. Small polarons are confined to a single (see Fig. 4.1) or a few lattice sites, large polarons can spread over tens of unit cells [65]. Motion characteristics of small and large polarons differs significantly. Coherent transport, which refers to carrier propagating through a medium with minimal scattering events and mobility above 1 $cm^2V^{-1}s^{-1}$, is a characteristic property of large polarons, while incoherent transport, where carrier propagation occurs as phonon-assisted hops with mobility below 1 $cm^2V^{-1}s^{-1}$, is indicative of small polarons [62]. Moreover, small polarons can become large if their mean-free-path becomes long. This implies that the lattice deformation induced by the presence of the polaron is spread out over larger volumes. A change in temperature can increase the mean-free-path of a small polaron. Likewise, large polarons can become small by losing coherence. Polaron formation and characteristics in halide perovskites can be controlled by volumetric strain and cation alloying in order to boost their performance in specific applications. The efficiency of halide perovskites in photovoltaic applications can be enhanced by minimizing non-radiative recombinations and the performance of the light-emitting applications can be amplified by maximizing the direct electron-phonon recombination of electrons and holes. Therefore, accurate modelling of polarons in halide perovskites is essential for understanding and improving their effectiveness in optoelectronic device architectures.

In lead-free halide perovskites such as $Cs_2AgBiBr_6$ polarons can have a significant impact on their electronic and optical properties. In **Paper I**, the formation of

polarons and their effect on the electronic properties of $Cs_2AgBiBr_6$ are examined. As presented in Fig. 4.2, excess charges can localize within lattice distortions. As discussed in Chapter 3, local distortions are important for modeling the electronic structure of halide perovskites. Also in the case of a polaron it is important to take the local distortions into account since its formation is found to be more favorable in the polymorphous network. Moreover, our findings revealed that the electron polaron formation is stable, whereas the hole polaron formation is marginally unstable in $Cs_2AgBiBr_6$ [66]. These self-trapped charges create in-gap states that can influence optical transitions, which can be used to interpret the PL signals in experimental studies [46].

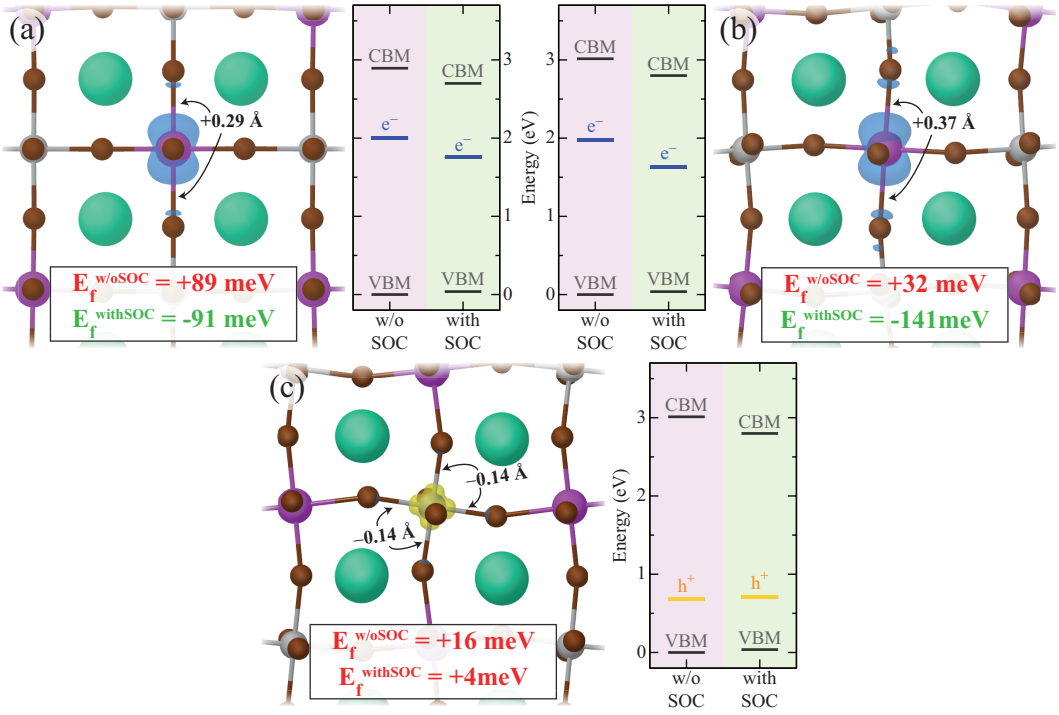

Figure 4.2: Band decomposed charge densities of polarons in $Cs_2AgBiBr_6$ in monomorphous and polymorphous structures. self-trapped excitons and holes are displayed by blue and yellow-colored isosurfaces, respectively. In the energy diagram, gray lines indicate VBM and CBM while yellow and blue lines show the hole and electron localized electronic states.

In **Paper III**, polaron landscape is examined in Germanium halide perovskite (GHP)s, in particular $CsGeX_3$ (X = Cl,Br,I). The results show that these materials exhibit polaron formation. Fig. 4.3 presents the polaronic configurations discovered in GHPs. While there are two stable configurations, EP1 and EP2, for the single electron polaron in $CsGeCl_3$, $CsGeBr_3$, and $CsGeI_3$, the single hole polaron is only

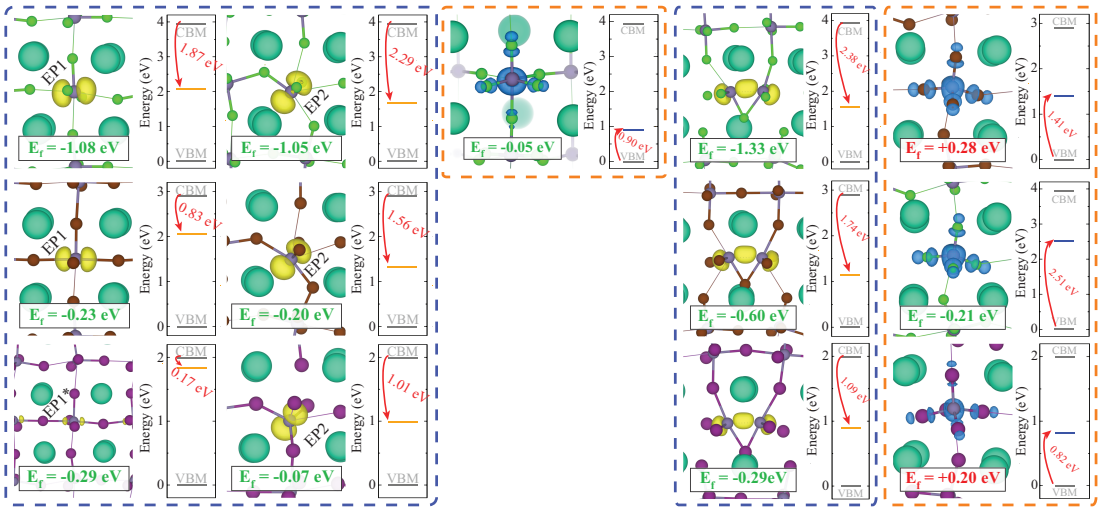

Figure 4.3: Isodensity surfaces of polaron configurations in $CsGeCl_3$, $CsGeBr_3$, and $CsGeI_3$. Electron and hole polarons are displayed by yellow and blue isosurfaces, respectively. In the energy diagram, gray lines indicate VBM and CBM while yellow and blue lines show the electron and hole localized electronic states. E_f shows the polaron formation energy per charge.

stable in $CsGeCl_3$. Moreover, the localization of multiple charge carriers in GHPs is also investigated. Results show that there is strong double electron polaron formation in all $CsGeX_3$ perovskites. However, in the case of double hole polaron, it is only stable in $CsGeCl_3$. In $CsGeBr_3$ and $CsGeI_3$, the polaron formation energy has a positive value, pointing out that these states are metastable double polarons.

4.2 Self-Trapped Excitons

An exciton is a bound state of an electron and hole that are attracted to each other by the Coulomb interaction. In halide perovskites different types of excitons, namely free, extrinsic, and intrinsic self-trapped excitons can occur. A free exciton is a neutral electron-hole quasiparticle that migrates almost freely through the lattice and is weakly affected by defects or impurities within the lattice. If excitons interact with defects or impurities, their mobility can be significantly reduced, and they can localize at these local lattice deformations, becoming extrinsic STEs. Additionally, excitons can localize without the presence of defects, due to transient lattice distortions, forming intrinsic STEs [67, 68]. A schematic illustration of the free exciton, as well as extrinsic and intrinsic STEs is shown in Fig. 4.4 along with a schematic configuration coordinate diagram.

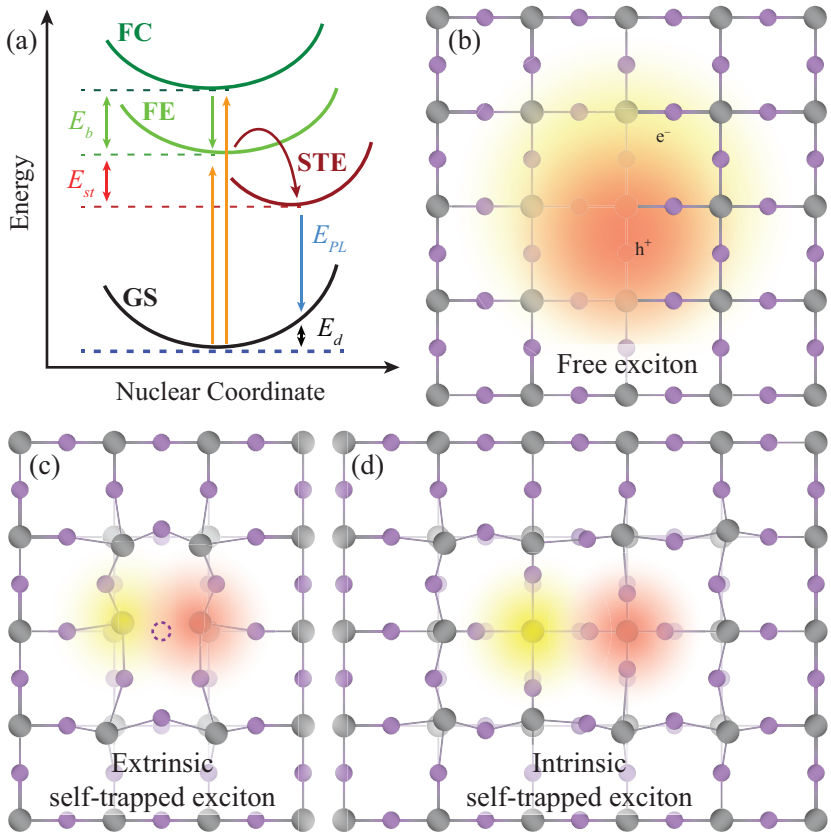

Figure 4.4: Schematic illustration of (a) the configuration coordinate diagram of the free carrier state (FC), free exciton state (FE), self-trapped exciton (STE), ground state (GS); crystal structures of (b) free exciton, (c) extrinsic self-trapped exciton, and (d) intrinsic self-trapped exciton.

Extrinsic self-trapped states can be induced by dopants. For example, Sn-doping in a 2D organic-inorganic halide perovskite is reported to generate a broadband red to near-infrared emission at room temperature originating from self-trapped states [69]. On the contrary, intrinsic self-trapped excitons do not require the presence of lattice defects. Intrinsic STEs can originate from the distorted excited states of octahedra and exhibit a broadband PL emission that covers most of the visible spectrum, as it is reported for $(C_4N_2H_{12})_2In_2Br_{10}$ [70]. While intrinsic self-trapped excitons cause homogenous emission broadening, extrinsic self-trapped excitons lead to in-homogeneous emission broadening due to the heterogeneity in the excited state [71]. Both intrinsic and extrinsic STEs are reported to be important features in halide perovskites and are leveraged in optoelectronic applications such as white-light generation [72–74].

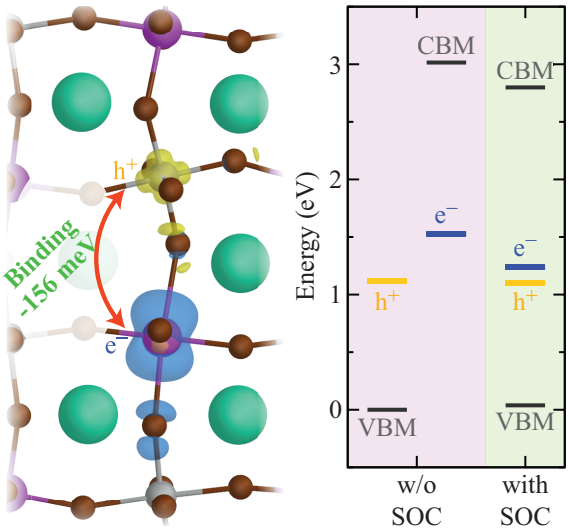

Figure 4.5: Isosurface with its binding energy of the self-trapped exciton in HDP $Cs_2AgBiBr_6$ and the corresponding energy diagram.

5

Computational Methods

In the previous chapters, the properties of metal halide perovskites that make them attractive semiconductors in wide-range of applications were examined, exploring both the advantages and limitations inherent in these materials. Moreover, findings on the structural dynamics and electronic structures of lead-free halide perovskites are presented. In this chapter, background on the used computational methods will be provided.

5.1 Electronic Structure Theory

The wavefunction of a quantum system contains information about the system dynamics. For non-relativistic systems, extracting this information involves solving the Schrödinger equation. However, when dealing with many-body interactions, complexity escalates dramatically, making the direct solution of the Schrödinger equation a formidable task. In order to overcome this problem, various computational strategies have been developed. Among these, DFT stands out due to its exceptional computational efficiency and accuracy in predicting a wide range of properties of many-electron systems.

The time-independent Schrödinger equation can mathematically illustrate the physical system as:

$$\hat{H}\Psi = E\Psi, \tag{5.1}$$

where $\hat{H}$ is the Hamiltonian operator, Ψ is the wave function, and E is the energy eigenvalue. The wavefunction Ψ describes nuclei and electrons in the system. The Hamiltonian for an N-body system can be divided into several parts:

$$\hat{H} = \hat{T}_n + \hat{T}_e + \hat{V}_{ne} + \hat{V}_{ee} + \hat{V}_{nn}, \tag{5.2}$$

where $\hat{T}_n$ is the kinetic energy of the nuclei, $\hat{T}_e$ is the kinetic energy of the electrons, $\hat{V}_{ne}$ is the interaction between nuclei and electrons, $\hat{V}_{ee}$ is the interaction between electrons, and $\hat{V}_{nn}$ is the Coulombic interaction between nuclei. The solution to the Schrödinger equation for an N-body system is non-trivial. Therefore, several approximations need to be introduced in order to simplify the problem. Granting that even the smallest nucleus is much heavier than an electron, the Born-Oppenheimer approximation separates the nuclear and electronic motions by assuming that the nuclear motion is much slower than the electronic motion. This allows electrons to be considered as responding instantaneously to any ionic changes. The separation of the nuclear and electronic degrees of freedom leads to the electronic Hamiltonian:

$$\hat{H}_e = \hat{T}_e + \hat{V}_{ne} + \hat{V}_{ee}. \tag{5.3}$$

Although the complexity is greatly reduced by the Born-Oppenheimer approximation, electron-electron repulsion introduces a many-body problem, making it formidable to find a solution to the Schrödinger equation for many-electron systems. An early approach to address this issue was the Hartree approximation. It simplifies the problem by treating each electron as moving independently in an averaged electric field created by all other electrons. This method neglects electron-electron correlations beyond the mean-field level, specifically the interactions due to their Coulombic repulsion.

The Hartree approximation has limitations. Neglecting electron-electron correlations beyond the mean-field level results in inaccuracies in the calculated electronic properties of a quantum system. Furthermore, treating each electron as moving independently neglects the antisymmetry requirement imposed by the Pauli exclusion principle, which ensures that no two electrons occupy the same quantum state. The limitations of the Hartree approximation can be addressed by more advanced theoretical methods.

5.2 Hartree-Fock Method

The HF method is an advancement over the Hartree approximation, providing a more refined approach for solving the many-electron problem. The wavefunction of an N-electron system is approximated as a single Slater determinant composed of single-electron wavefunctions, which obeys the Pauli exclusion principle:

$$\Psi(r) = \frac{1}{\sqrt{N!}} \begin{vmatrix} \psi_1(x_1) & \psi_2(x_1) & ... & \psi_N(x_1) \\ \psi_1(x_2) & \psi_2(x_2) & ... & \psi_N(x_2) \\ \vdots & \vdots & & \vdots \\ \psi_1(x_1) & \psi_2(x_1) & ... & \psi_N(x_1) \end{vmatrix}, \tag{5.4}$$

where $\psi_i(x_i)$ are the spin orbitals composed of the spatial orbital function and the spin function. The HF method neglects the electron correlation. The Hartree-Fock equation that solves the Schrödinger equation to determine the molecular orbitals is:

$$F_i\psi_i = [-\frac{1}{2}\nabla_i^2 - \sum_i \frac{Z_i}{|r_i - R_i|} + \sum_j (J_j - K_j)]\psi_i, \tag{5.5}$$

where F_i is the Fock operator that represents the effective one-electron operator experienced by an electron in the molecular orbital ψ_i, J_j is the Coulomb operator, K_j is the exchange operator. They can be mathematically described as:

$$J_j\psi_i(x_2) = \langle\psi_j(x_1)|\frac{1}{|x_1 - x_2|}|\psi_j(x_1)\rangle\psi_i(x_2), \quad \text{and} \tag{5.6}$$

$$K_j\psi_i(x_2) = \langle\psi_j(x_1)|\frac{1}{|x_1 - x_2|}|\psi_i(x_1)\rangle\psi_j(x_2). \tag{5.7}$$

Solving the HF equations in (Eq. 5.4) for an initial guess of molecular orbitals results in the change in the Fock operator F_i. The HF equations are solved iteratively until convergence is reached. This solution is referred to as the self-consistent field solution.

5.3 Density Functional Theory

Another approach to solving the many-body Schrödinger equation is DFT, which is a widely used computational method. It provides an efficient and effective framework for calculating the electronic properties of many-body systems. DFT uses the electron density as its fundamental variable, based on the Hohenberg-Kohn theorems. The first theorem states that the external potential, $V_{\text{ext}}(r)$ is in correspondence with the functional of the electron density $n(r)$. According to the second theorem, the system's energy can be calculated using the electron density functional. The exact ground state density, labeled as $n_0(r)$, minimizes the total energy of the system, yielding the true ground-state energy. The ground state energy is obtained as the expected value of the Hamiltonian using the ground state wave function:

$$E_{\mathrm{HK}}[n] = \frac{\langle \Psi_0 | H | \Psi_0 \rangle}{\langle \Psi_0 | \Psi_0 \rangle} \equiv \langle H \rangle = \langle T \rangle + \int d^3\mathbf{r} V_{\mathrm{ext}}(\mathbf{r}) n_0(\mathbf{r}) + \langle V_{\mathrm{int}} \rangle + E_{II}, \quad (5.8)$$

where E_{II} represents the interaction energy of the nuclei.

Forces on a nucleus can be calculated based on the Hellmann-Feynman theorem. This theorem is crucial for structural optimization, with the force on a nucleus represented as:

$$\mathbf{F}_I = -\frac{\partial E}{\partial \mathbf{R}_I}. \quad (5.9)$$

The total energy, derived from Eq. 5.8, informs the computation about the force on the nucleus as follows:

$$\mathbf{F}_I = -\int d^3\mathbf{r} n(\mathbf{r}) \frac{\partial V_{\mathrm{ext}}(\mathbf{r})}{\partial \mathbf{R}_I} - \frac{\partial E_{II}}{\partial \mathbf{R}_I}. \quad (5.10)$$

Building on the Hohenberg-Kohn theorems, the Kohn-Sham formalism provides a method to approximate the energy functional by introducing non-interacting reference electrons that reproduce the same electron density as the real system. The energy functional is expressed as:

$$E[n] = \int n(\mathbf{r}) V_{\mathrm{ext}}(\mathbf{r}) dr + F_{\mathrm{HK}}[n] \; = \int n(\mathbf{r}) V_{\mathrm{ext}}(\mathbf{r}) dr + T[n] + E^{\mathrm{Hartree}}[n] + E_{\mathrm{xc}}[n]. \quad (5.11)$$

In this expression, F_{HK} is the universal functional, $T[n]$ represents the kinetic energy of non-interacting electrons, $E^{\mathrm{Hartree}}[n]$ is the Hartree energy, and $E_{\mathrm{xc}}[n]$ denotes the exchange and correlation energy. The effective potential is defined as:

$$V^{\mathrm{eff}} = \frac{\delta \int n(\mathbf{r}) V_{\mathrm{ext}}(\mathbf{r}) d\mathbf{r} + E^{\mathrm{Hartree}}[n] + E_{\mathrm{xc}}[n]}{\delta n(r)}. \quad (5.12)$$

This equation simplifies to:

$$V^{\mathrm{eff}} = V_{\mathrm{ext}}(\mathbf{r}) + \int \frac{n(\mathbf{r}')}{|\mathbf{r} - \mathbf{r}'|} d\mathbf{r}' + V_{\mathrm{xc}}(\mathbf{r}) \quad (5.13)$$

where $V_{\mathrm{xc}}(\mathbf{r})$ is the exchange-correlation potential. Utilizing this form of effective potential, the Kohn-Sham DFT Schrödinger equation models a one-electron system, yielding the electron density:

$$\left[-\frac{1}{2}\nabla^2 + V^{\text{eff}}\right]\phi_i = E_i\phi_i. \tag{5.14}$$

Here, ϕ_i are the Kohn-Sham one-electron orbital eigenfunctions. The electron density is determined from Eq. 5.14 as:

$$n(\mathbf{r}) = \sum_{i=1}^{N} |\phi_i|^2. \tag{5.15}$$

The effective potential, V_{eff}, depends on the density $n(\mathbf{r})$. To solve the Kohn-Sham equations, an initial guess on the electron density is made. The corresponding effective potential (V_{eff}) is constructed, the Kohn-Sham orbitals (ϕ_i) are calculated, and the new electron density derived from these orbitals is compared with the initial density. Upon reaching convergence in this self-consistent process, the final electron density can be used to calculate the total energy. Although this process determines the final electron density, the exact exchange-correlation energy remains unknown.

5.3.1 Exchange-Correlation Functionals

The Kohn-Sham equations, integral to DFT, are employed to ascertain the final electron density of a system, which is then used to calculate the total energy. However, to complete these equations, the exchange-correlation energy E_{xc} is essential but not directly available. Approximations are made to estimate this energy, and these approximations, known as exchange-correlation functional, are a fundamental aspect of DFT.

The Local Density Approximation (LDA) treats the system as consisting of finite volumes, each with a constant electron density. The exchange-correlation energy in LDA is given by:

$$E_{\text{xc}}^{\text{LDA}}[n] = \int n(\mathbf{r})\epsilon_{\text{xc}}^{\text{unif}}[n]d\mathbf{r} \tag{5.16}$$

Here, $\epsilon_{\text{xc}}^{\text{unif}}$ is the exchange-correlation energy per electron [75]. LDA is particularly effective in systems such as metals where the electron density changes smoothly. However, it generally tends to underestimate lattice parameters and overestimate cohesive energies.

The Generalized Gradient Approximation (GGA) goes a step further by accounting for variations in electron density gradients within each division. The GGA expression for exchange-correlation energy is:

$$E_{\text{xc}}^{\text{GGA}}[n] = \int f^{\text{GGA}}(n(\mathbf{r}), \nabla n(\mathbf{r}))d\mathbf{r}. \tag{5.17}$$

In this equation, $\nabla n(\mathbf{r})$ represents the gradient of the electron density [76]. Unlike LDA, GGA is more accurate for systems with rapidly changing electron densities, often yielding results with higher precision. Over time, several GGA functionals were constructed by applying gradient corrections in various ways. Perdew-Wang (PW91) [77], Perdew-Burke-Ernzerhof (PBE) [76], and revised PBE for solids (PBEsol) [78] are the examples of commonly used GGA functionals.

Both LDA and GGA experience problems describing the electronic structure of semiconductors that arise from inaccurate description of systems with fractional charges [79, 80]. Therefore, they cannot properly describe localized states. Moreover, they tend to drastically underestimate the band gap of a system due to the self-interaction error, where an electron interacts with itself through the Coulomb (Hartree) term. This error arises because the exchange-correlation functionals such as LDA and GGA do not fully cancel out the self-interaction. In order to treat these problems, several approaches have been used. One of these approaches is to use hybrid functionals [80–82].

Hybrid functionals have gained popularity for determining exchange-correlation energy. They are typically linear combinations of other known exchange-correlation functionals. Hybrid functionals can provide results closer to the experimental values, therefore improving the accuracy of the calculations while increasing the computational cost. A well-known hybrid-functional, PBE0, is a combination of PBE and a portion (0.25) of the exact exchange from Hartree-Fock theory [82–84]. The mathematical expression for PBE0 is:

$$E_{\mathrm{xc}}^{\mathrm{PBE0}} = \frac{1}{4}E_x^{\mathrm{HF}} + \frac{3}{4}E_x^{\mathrm{PBE}} + E_c^{\mathrm{PBE}}. \tag{5.18}$$

Moreover, based on the PBE0 approach, PBE0(α) hybrid functionals can be derived by changing the mixing parameter of the Fock exchange. It is reported that a *fine-tuned* PBE0(α) functional can give highly accurate electronic structures, comparable with computationally demanding GW [85]. The mathematical expression follows:

$$E_{\mathrm{xc}}^{\mathrm{PBE0}(\alpha)} = \alpha E_x^{\mathrm{HF}} + (1-\alpha)E_x^{\mathrm{PBE}} + E_c^{\mathrm{PBE}}, \tag{5.19}$$

where α is the fraction of Fock exchange. The *fine-tuned* α value is specific for a system, which improves the accuracy by correction of the self-interaction error [86]. The fraction of the HF exchange energy can be derived by enforcing the Koopmans' condition [85]. The generalized Koopmans' theorem implies that the total energy of a system should be piece-wise linear upon the addition of electrons [87]. That implies that the single-particle level, ϵ_i, is constant and does not depend on its occupation. Fig. 5.1 illustrates the variation of single-particle levels with α. The eigenvalues intersect at the point where α satisfies the Koopmans' condition. At

this fraction α, self-interaction error is minimized for the system. The generalized Koopmans' theorem is beneficial when it comes to correctly describing localized states such as polarons in semiconductors where electron-phonon interactions are significant.

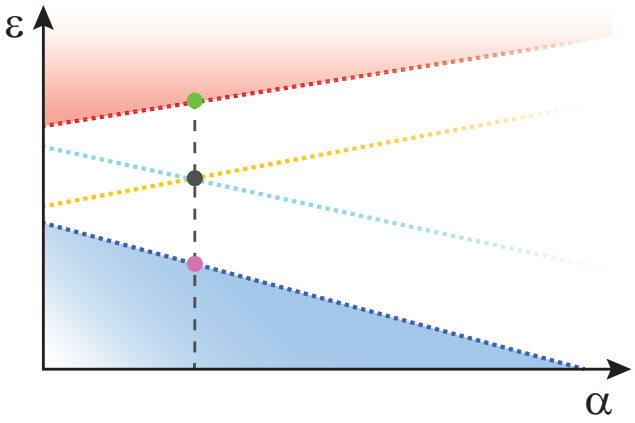

Figure 5.1: Illustration of single-particle levels vary with Fock exchange fraction in the hybrid functional. Blue and red regions indicate occupied and unoccupied bands, respectively. Dashed blue and red lines show the band edges, VBM and CBM, respectively. Light blue and orange dashed lines display occupied and unoccupied single-particle levels.

5.4 Molecular Dynamics

Materials simulations are often carried out at 0 K, for fixed atomic positions. However, properties of materials at finite temperatures can exhibit significantly different behavior due to thermal vibrations and dynamic interactions between atoms. Molecular Dynamics (MD) simulations are a powerful tool for capturing these phenomena. In this thesis, I use MD simulations to examine phase transitions in halide perovskites.

MD simulations involve solving the equations of motion, which describe the trajectories of particles over time based on the forces acting on them:

$$m_I \frac{\partial^2 \mathbf{r}_I(t)}{\partial t^2} = F_I(t), \tag{5.20}$$

where m_I is the mass of the atom I, $\mathbf{r}_I(t)$ is the position of the atom I at time t, and $F_I(t)$ is the force acting on it. These forces are derived from the total potential energy of the system, U, which can be written as:

$$U = U(\{\mathbf{r}_I(t)\}), \tag{5.21}$$

where $\{\mathbf{r}_I(t)\}$ represents the set of positions of all atoms at time t. The forces acting on each atom are obtained by taking the negative gradient of the potential energy with respect to the atomic positions:

$$\mathbf{F}_I(t) = -\nabla_I U(\{\mathbf{r}_I(t)\}). \tag{5.22}$$

In *ab initio* Molecular Dynamics (AIMD), the potential energy, U, is determined from first-principles calculations. The time evolution of the system is performed in increments, referred to as time steps, denoted by Δt. At each time step, AIMD uses quantum mechanical methods such as DFT to calculate the electronic structure of the system, which provides the forces acting on atoms. This approach allows for accurate, real-time description of atomic interactions including complex effects such as bond-breaking and charge localization. As a result, AIMD is a reliable method in which no assumptions about the system need to be made *a priori*. However, AIMD is computationally expensive since the electronic structure is recalculated at every time step for each atomic configuration, which limits its use to relatively small systems and short time scales.

In contrast to AIMD, in MD simulations based on parametrized interatomic potentials the forces between atoms are approximated. These interatomic potentials are mathematical functions that are parameterized based on simplified physical models or experimental data to describe how the atoms in a system interact. Computing forces from these parametrized interatomic potentials is computationally much cheaper than performing the on-the-fly electronic structure calculations in AIMD, enabling simulations of much larger systems over longer time scales.

Among these approaches, classical MD fully neglects quantum nuclear effects, and treats atomic motion using Newtonian mechanics. While computationally efficient, its accuracy heavily depends on the choice of the interatomic potential. Empirical potentials may not be able to fully capture the true nature of interatomic interactions, especially where the electronic effects play a significant role. In recent years, machine learning techniques allowed for bridging between the accuracy of AIMD and the efficiency of classical MD. Based on a limited dataset of DFT calculation, one can construct machine-learned interatomic potentials that retain the predictiveness of AIMD at a fraction of the cost. Here, I used machine-learned potentials to investigate phase transitions in HDPs.

All MD simulations output atomic trajectories. The integration method used at each time step is determined by the numerical algorithm (e.g., Verlet or velocity-Verlet). The velocity-Verlet algorithm, often used due to its stability, updates velocities and positions as follows:

$$v_I(t_{m+1}) = v_I(t_m) + \frac{F_I(t_m) + F_I(t_{(m+1)})}{2m_I}\Delta t \quad \text{and} \tag{5.23}$$

$$r_I(t_{m+1}) = \mathbf{r}_I(t_m) + v_I(t_m)\Delta t + \frac{1}{2}\frac{F_I(t_m)}{m_I}(\Delta t)^2, \tag{5.24}$$

where $v_I(t_{m+1})$, and $v_I(t_m)$ are the velocities, $r_I(t_{m+1})$ and $\mathbf{r}_I(t_m)$ are atomic positions of atom I at time steps t_m and t_{m+1}, respectively. The choice of ensemble dictates the control of factors such as temperature and pressure, which can be controlled through thermostats and barostats. Commonly used ensembles in MD simulations include NVE, NVT, and NPT.

In the micro-canonical NVE ensemble, the number of particles (N), volume (V), and energy (E) are constant. In the canonical NVT ensemble, number of particles, volume, and temperature (T) are kept constant. The control over temperature is achieved through the use of *thermostats*. Several thermostats can be used with the NVT ensemble to modulate the temperature. Some commonly used thermostats are Berendsen, Langevin, and Nose-Hoover thermostats [88–91].

Finally, in the isothermal-isobaric NPT ensemble *barostats* are used to control the pressure within the simulation cell. Berendsen and stochastic cell rescaling barostats are some of the commonly used ones [88, 92]. In **Paper II**, the NPT ensemble and the stochastic cell rescaling barostat are used.

5.5 Neuroevolution Machine Learning Potentials

Among various machine learning-based interatomic potentials, Neuroevolution Potential (NEP)s have emerged as an accurate and efficient approach. NEPs use ANN to model interatomic interactions. This section first introduces ANNs, then describes the generation of NEPs.

An ANN is a computational model that is inspired by the structure of the human brain, consisting of neurons and synapses [93]. Neurons process the input data, apply a function, and pass the output to subsequent layers. The structure of an ANN typically includes an input layer, one or more hidden layers, and an output layer. The hidden layer, consisting of neurons positioned between the input and output layers, plays a crucial role in transforming the input data into an expression that the output layer can use. ANNs are involved in a learning process where the weights of the connections between neurons are adjusted to minimize the difference between their predicted output and the actual output. Although there are several types of ANNs, this chapter focuses specifically on feed-forward neural networks.

Neuroevolution machine learning potentials are trained using an evolutionary strategy for performing high accuracy and low-cost atomistic simulations [94, 95]. A feed-forward neural network is used to extract features such as site energy of an atom as a vector that has N_{des} components, which is referred to as a descriptor vector. Such an ANN can be mathematically described as,

$$U_i(\mathbf{q}) = U_i(\{\mathbf{q}_v^i\}_{v=1}^{N_{\rm des}}). \tag{5.25}$$

With a single hidden layer, the neural network model becomes:

$$U_i = \sum_{\mu}^{N_{\rm neu}} w_\mu^{(1)} \tanh\left(\sum_{v=1}^{N_{\rm des}} w_{\mu v}^{(0)} q_v^i - b_\mu^{(0)}\right) - b^{(1)}, \tag{5.26}$$

where $\tanh(x)$ is the activation function in the hidden layer, $w_{\mu v}^{(0)}$ is the connection weight matrix from the input layer to the hidden layer, $w_\mu^{(1)}$ is the connection weight vector from the hidden layer to the output node, $b^{(0)}$ is the bias vector of the hidden layer, and $b^{(1)}$ is the bias node for U_i. Here, $w_{\mu v}^{(0)}$, $w_\mu^{(1)}$, $b^{(0)}$, and $b^{(1)}$ are trainable parameters. An important aspect of machine learning potentials is the use of descriptors. The descriptor in a neuroevolution potential is an abstract vector that consists of radial and angular parts. Descriptors that contain only the radial information, or both the radial and angular information, are referred to as radial or angular descriptors, respectively. The radial descriptor components are defined as:

$$q_n^i = \sum_{j!=i} g_n(r_{ij}), \tag{5.27}$$

where $g_n(r_{ij})$ is the contribution from each neighbour. The summation runs over all the neighbors of atom i.

In order to train a NEP model, one needs to have a comprehensive training dataset, $\mathcal{D}_i$, that covers the relevant configuration space. In the approach used here, the initial dataset, $\mathcal{D}_0$, is composed of a variation of rattled and strained structures. This initial set is a good start for capturing the potential energy surface of the system. Then, an ensemble of models is trained on several random subsets of the dataset $\mathcal{D}_0$, along with a full potential trained on all data. Each model in the ensemble is trained on a different random subset of the data, therefore reducing the risk of overfitting. This method is called Bootstrap aggregating (bagging) [96]. After training the ensemble, a short MD simulation is performed using the full model. Forces in snapshots from the MD runs are predicted by each model in the ensemble. The uncertainty for each structure is then estimated by calculating the standard deviation of the forces predicted by different models. The model is improved by using the **active learning** approach, which iteratively enhances $\mathcal{D}_i$ by identifying and collecting atomic configurations where the model exhibits high uncertainty. These collected configurations with high uncertainty are recalculated using DFT. New data points are added to the training set, yielding an updated dataset, $\mathcal{D}_{i+1}$. This active learning cycle is repeated multiple times (typically 3-10 times). Each time, a new ensemble of models is trained on the expanded dataset $\mathcal{D}_i$,

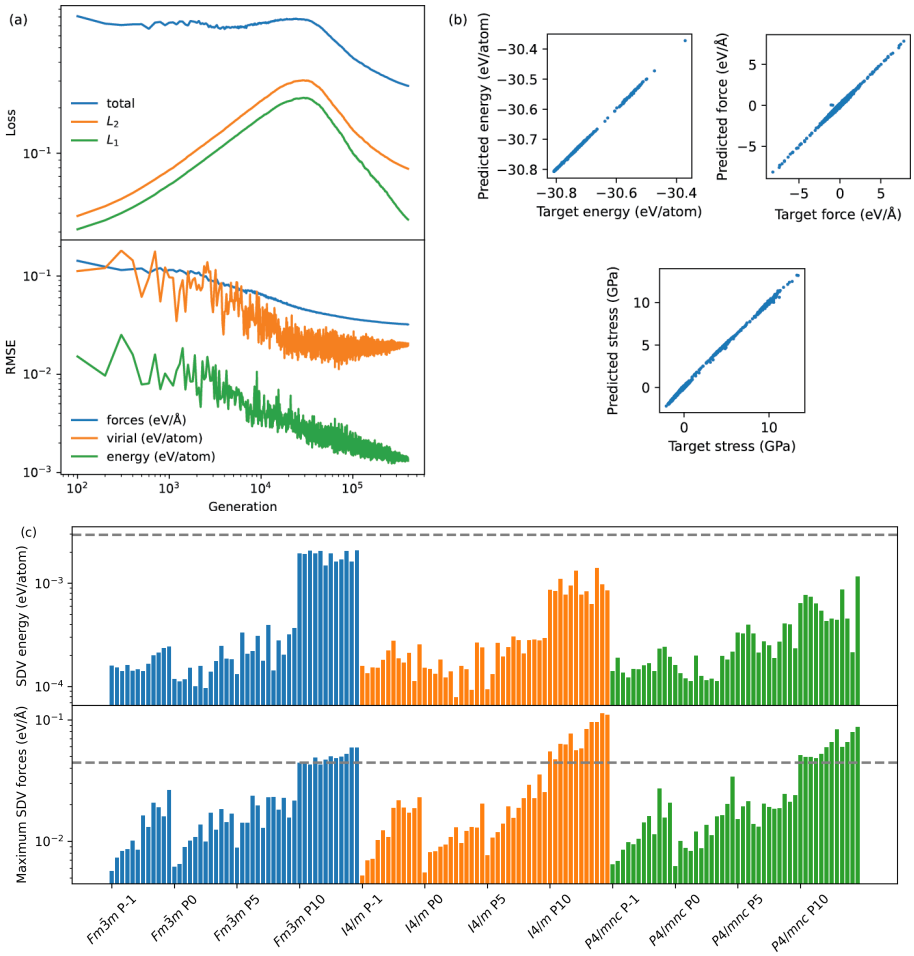

Figure 5.2: (a) Evolution of total loss and its individual contributions during training of the full model for $Cs_2AgBiBr_6$ based on the SCAN-rVV10 functional. (b) Parity plots for the full model for $Cs_2AgBiBr_6$. (c) Energy and force RMSE for the uncertainties.

followed by MD simulation and updating the dataset with new high-uncertainty structures (see in Fig. 5.2 (c)). The process continues until the uncertainty in the forces and energies of the structures determined during MD falls below the overall force RMSE and energy RMSE for the dataset. This iterative scheme significantly improves the accuracy of the trained NEP model while keeping the computational cost low.

6

Summary of papers

Paper I

Charge Localization in $Cs_2AgBiBr_6$ Double Perovskite: Small Polarons and Self-Trapped Excitons

$Cs_2AgBiBr_6$ is a lead-free halide double perovskite that exhibits intriguing optoelectronic properties such as a long-lived charge carrier lifetime and a relatively narrow band gap within the visible spectrum, making it suitable for photovoltaic applications, photocatalysis, photodetectors, and X-ray detectors. Understanding charge localization in this material is crucial, as self-trapped charges can impact the charge transport and optical properties. In **Paper I**, charge localization phenomena are studied in the halide double perovskite $Cs_2AgBiBr_6$. This material is cubic at room temperature, however, the highly symmetric structure is not stable at 0K, at which electronic structure calculations are generally performed. We carried out DFT calculations at the PBE0(α) level (at 0 K), where the fraction of Hartree-Fock exchange, α, is determined that satisfies Koopmans' theorem. The study reveals the importance of self-trapped states in this material, highlighting it as a crucial factor for accurate modeling of localized charges in $Cs_2AgBiBr_6$.

The findings from this study indicate that electron localization on Bi atoms is energetically favorable, whereas hole polarons at Ag sites are marginally unstable. Moreover, the attraction between oppositely charged polarons at neighboring Ag and Bi sites results in the formation of STEs. Furthermore, the inclusion of spin-orbit coupling effects in the analysis is crucial for understanding the charge behavior and the stabilization effect of neighboring electron and hole localizations in forming STEs. Results are compared with a recent experimental publication by Wright *et al.* [46], particularly in relation to PL measurements. Experiments indicate

barrier-less self-trapping of charges, evident from a PL signal around 1.9 eV, which is thought to correspond to a localized color center which can arise due to presence of defects. We suggest that several possible scenarios can explain the observed PL signal. This includes direct recombination within the STE, the recombination of a trapped electron with a delocalized hole, and the recombination of a hole trapped in the STE with a delocalized electron in the conduction band. Results in this work contribute significantly to the understanding of charge localization mechanisms in $Cs_2AgBiBr_6$, offering insights that are valuable for the development and optimization of green optoelectronic devices.

Paper II

Effects of Lone-Pair Electrons on the Octahedral Tilting in Halide Double Perovskites

Halide Double Perovskite can contain different combinations of metals. It has been suggested that the structure and dynamics of these materials are related to the presence of lone-pair electrons. In **Paper II**, a comprehensive investigation is conducted on how lone-pair electrons affect the structural dynamics and phase transition energetics in halide double perovskites. The tilting energy and angles at 0 K are calculated for 46 HDPs in cubic $Fm\bar{3}m$ ($a^0a^0a^0$), tetragonal $I4/m$ ($a^0a^0c^-$), and tetragonal $P4/mnc$ ($a^0a^0c^+$) phases. It is revealed that HDPs with two lone-pair electrons tend to exhibit significant octahedral tilting, favoring tetragonal structures over cubic. In contrast, HDPs with one lone-pair electron show varied trends in tilting angles, indicating that phase stability and tilting in that class strongly depend on additional factors. Furthermore, HDPs without lone-pair electrons generally adopt cubic symmetry already at 0 K, although there are notable exceptions.

Furthermore, to directly assess the relationship between the degree of tilting at 0 K and phase transitions, the neuroevolution potentials are trained for two representative cases, $Cs_2AgBiBr_6$ and Cs_2AgBiI_6. Heating and cooling MD runs are carried out. The results show that the material with stronger tilting at 0 K transitions at significantly higher temperatures. $Cs_2AgBiBr_6$ shows a single tetragonal-to-cubic transition around 70 K, while Cs_2AgBiI_6 displays two phase transitions, one at 120 K (monoclinic-to-tetragonal), and another at 210 K (tetragonal-to-cubic). This approach highlights the trend of how octahedral tilting evolves with temperature and its role in driving structural phase transitions in HDPs. These results deepen the understanding of phase transitions in HDPs and the role of lone-pair electrons related to the B-site cations, which is essential for developing more stable and efficient materials.

Paper III

Exploring the Polaron Landscape in Lead-Free Germanium Halide Perovskites: $CsGeCl_3$, $CsGeBr_3$, and $CsGeI_3$

Germanium halide perovskites ($CsGeCl_3$, $CsGeBr_3$, and $CsGeI_3$) are non-toxic alternatives to lead-based halide perovskites. These materials exhibit broad-range absorption in the UV-visible spectrum and direct bandgaps tunable over the entire visible range through strain engineering, piezoelectric responses, and metal doping. GHPs have been used in various applications including solar cells, lasers, and infrared photodetectors. GHPs are a promising group of materials in nonlinear optics. Localized charge carriers such as polarons can influence the nonlinear optical responses in these materials, therefore it is important to understand the excited state behavior. In **Paper III**, polarons in $CsGeX_3$ are studied. These materials adopt a monoclinic phase with Cc space group at low temperatures. DFT calculations are carried out at the PBE0(α) level (at 0 K), where α values are the fraction of the exact exchange that satisfies Koopmans' condition. The study explores various configurations of self-trapped states, reporting single- and double-polaron formation in GHPs.

The findings from this study indicate that single electron polarons in all $CsGeX_3$ perovskites are stable, while the single hole polaron is only stable in $CsGeCl_3$. Moreover, GHPs exhibit favorable double electron polaron formation. However, in the case of the double hole polaron configuration, only $CsGeCl_3$ is energetically stable. In $CsGeBr_3$ and $CsGeI_3$, although double hole polarons configurations can be identified, their formation is energetically unfavorable. Results in this work contribute to the understanding of charge localization mechanisms in $CsGeX_3$ perovskites, providing valuable insights for their future applications.

7

Conclusions and Outlook

In this thesis, a computational investigation of lead-free halide perovskites is conducted. The focus is primarily on the halide double perovskites and $CsGeX_3$ single perovskites. Initially, the composition of these lead-free alternatives – which offer tunability, increasing their potential for future optoelectronic applications – is examined. However, composition alone does not determine the electronic structure of these semiconductors. This leads to the main focus of the thesis; structural dynamics, phase transitions, and formation of self-trapped states in lead-free halide perovskites.

In the context of the structural properties of lead-free perovskites, various structural phases were explored, focusing on the effects of octahedral tilting. Among 15 possible tilt systems, the cubic and tetragonal phases characterized by Glazers' notation $a^0a^0a^0$, $a^0a^0c^+$, and $a^0a^0c^-$ were examined in relation to the number of lone-pair electrons. The findings were revealed a distinct correlation between the number of lone-pair electrons in the unit cell and the tilt angles. Additionally, the investigation was extended to local structural distortions, examining how temperature affects the structural dynamics in halide double perovskites through MD simulations. To achieve DFT-level accuracy while minimizing the computation demand, NEPs were trained and employed. The phase diagrams are constructed for the selected HDPs to correlate with the predicted effect of the number of lone-pair electrons on the magnitude of tilts.

Additionally, charge localization in lead-free halide perovskites is was investigated. The importance of the formation of polarons and STEs in lead-free halide perovskites was highlighted. Overall, this thesis offers significant insights into the behavior of localized charges such as polarons and STEs, along with an in-depth understanding of phase transitions and tilting instabilities in these materials.

Future work may explore the open questions that emerge from the papers pre-

sented in this thesis. For **Paper II**, further investigation could focus on identifying additional factors that influence octahedral tilting in perovskites that have one lone-pair electron. To achieve this goal, machine-learning based feature selection algorithms could be used. In **Paper I**, I have examined localized charges in the bulk material. However, understanding the behavior of self-trapped states at the material's surfaces is also important. Therefore, charge localization on the $Cs_2AgBiBr_6$ surface could be further examined. In **Paper III**, I studied the formation of electron and hole polarons in $CsGeX_3$ (X=Cl,Br,I). Future work could extend the scope to STEs in these materials. Given the potential interplay between polarons and STEs, understanding the formation mechanism of STEs in $CsGeX_3$ could improve their performance in non-linear optics. Furthermore, STEs should also be investigated in other HDPs, as some of them can be prone to charge localization. One of the interesting cases is $Cs_2AgInCl_6$, where experimental studies report temperature-dependent optical response. It would be interesting to investigate charge localization dynamics under varying thermal conditions to understand the process behind the thermal quenching of luminescence in this perovskite material.

Acknowledgments

First and foremost, I would like to express my deepest gratitude to my supervisor, Julia Wiktor, for all your support, guidance, and boundless patience in this last three years. This thesis would not have been possible without your mentorship and encouragement.

I would like to thank my examiner, Paul Erhart, for your insightful feedback and suggestions. My sincere thanks also go to my assistant supervisor, Matthias Geilhufe.

I would like to extend my thanks to my coworkers at the CMMT division for providing a fun and friendly work environment. Your friendship made my time here enjoyable and memorable.

Last but not least, a special thanks to my wife, Paulina, for always being by my side, supporting me through every challenge, and believing in me. To our son, Adam, thank you for bringing endless joy into my life. You inspire me every day.

Bibliography

[1] A. Kojima, K. Teshima, Y. Shirai, and T. Miyasaka, *Organometal halide perovskites as visible-light sensitizers for photovoltaic cells,* Journal of the American Chemical Society **131**, 6050 (2009).

[2] S. D. Stranks and H. J. Snaith, *Metal-halide perovskites for photovoltaic and light-emitting devices,* Nature Nanotechnology **10**, 391 (2015).

[3] Y. Fu, H. Zhu, J. Chen, M. P. Hautzinger, X.-Y. Zhu, and S. Jin, *Metal halide perovskite nanostructures for optoelectronic applications and the study of physical properties,* Nature Reviews Materials **4**, 169 (2019).

[4] M. Jeong, I. W. Choi, E. M. Go, Y. Cho, M. Kim, B. Lee, S. Jeong, Y. Jo, H. W. Choi, J. Lee, J.-H. Bae, S. K. Kwak, D. S. Kim, and C. Yang, *Stable perovskite solar cells with efficiency exceeding 24.8% and 0.3-V voltage loss,* Science **369**, 1615 (2020).

[5] M. A. Green, E. D. Dunlop, M. Yoshita, N. Kopidakis, K. Bothe, G. Siefer, and X. Hao, *Solar cell efficiency tables (Version 63),* Progress in Photovoltaics: Research and Applications **32**, 3 (2024).

[6] Z. Li, T. R. Klein, D. H. Kim, M. Yang, J. J. Berry, M. F. Van Hest, and K. Zhu, *Scalable fabrication of perovskite solar cells,* Nature Reviews Materials **3**, 1 (2018).

[7] N.-G. Park, *Research direction toward scalable, stable, and high efficiency perovskite solar cells,* Advanced Energy Materials **10**, 1903106 (2020).

[8] X. Chen, H. Xiang, R. Wang, Y. Wang, Y. Wang, and H. Zeng, *Perovskite-Organic Coupling WLED: Progress and Perspective,* Advanced Functional Materials , 2304750 (2023).

[9] S. Chen, J. Lin, S. Zheng, Y. Zheng, and D. Chen, *Efficient and Stable Perovskite White Light-Emitting Diodes for Backlit Display,* Advanced Functional Materials , 2213442 (2023).

[10] V. R. Schröder, N. Fratzscher, N. Z. Morales, D. S. Rühl, F. Hermerschmidt, E. L. Unger, and E. J. List-Kratochvil, *Bicolour, large area, inkjet-printed metal halide perovskite light emitting diodes,* Materials Horizons , (2024).

[11] M.-A. Stoeckel, M. Gobbi, S. Bonacchi, F. Liscio, L. Ferlauto, E. Orgiu, and P. Samorì, *Reversible, fast, and wide-range oxygen sensor based on nanostructured organometal halide perovskite,* Advanced Materials **29**, 1702469 (2017).

[12] M. J. Seol, S. H. Hwang, J. W. Han, H. W. Jang, and S. Y. Kim, *Recent Progress of Halide Perovskites Applied to Five Senses Sensors,* ACS Applied Electronic Materials , (2023).

[13] P. Billen, E. Leccisi, S. Dastidar, S. Li, L. Lobaton, S. Spatari, A. T. Fafarman, V. M. Fthenakis, and J. B. Baxter, *Comparative evaluation of lead emissions and toxicity potential in the life cycle of lead halide perovskite photovoltaics,* Energy **166**, 1089 (2019).

[14] M. Ren, X. Qian, Y. Chen, T. Wang, and Y. Zhao, *Potential lead toxicity and leakage issues on lead halide perovskite photovoltaics,* Journal of Hazardous Materials **426**, 127848 (2022).

[15] B.-w. Park and S. I. Seok, *Intrinsic instability of inorganic–organic hybrid halide perovskite materials,* Advanced Materials **31**, 1805337 (2019).

[16] P. Bhatt, A. K. Pandey, A. Rajput, K. K. Sharma, A. Moyez, and A. Tewari, *A review on computational modeling of instability and degradation issues of halide perovskite photovoltaic materials,* Wiley Interdisciplinary Reviews: Computational Molecular Science **13**, e1677 (2023).

[17] Y. Jiang, L. Qiu, E. J. Juarez-Perez, L. K. Ono, Z. Hu, Z. Liu, Z. Wu, L. Meng, Q. Wang, and Y. Qi, *Reduction of lead leakage from damaged lead halide perovskite solar modules using self-healing polymer-based encapsulation,* Nature Energy **4**, 585 (2019).

[18] Z. Xiao, Z. Song, and Y. Yan, *From lead halide perovskites to lead-free metal halide perovskites and perovskite derivatives,* Advanced Materials **31**, 1803792 (2019).

[19] T. C. Jellicoe, J. M. Richter, H. F. J. Glass, M. Tabachnyk, R. Brady, S. E. Dutton, A. Rao, R. H. Friend, D. Credgington, N. C. Greenham, and M. L. Böhm, *Synthesis and optical properties of lead-free cesium tin halide perovskite nanocrystals,* Journal of the American Chemical Society **138**, 2941 (2016).

[20] H.-H. Fang, S. Adjokatse, S. Shao, J. Even, and M. A. Loi, *Long-lived hot-carrier light emission and large blue shift in formamidinium tin triiodide perovskites,* Nature Communications **9**, 243 (2018).

[21] C. C. Stoumpos, C. D. Malliakas, and M. G. Kanatzidis, *Semiconducting tin and lead iodide perovskites with organic cations: phase transitions, high mobilities, and near-infrared photoluminescent properties,* Inorganic Chemistry **52**, 9019 (2013).

[22] N. K. Noel, S. D. Stranks, A. Abate, C. Wehrenfennig, S. Guarnera, A.-A. Haghighirad, A. Sadhanala, G. E. Eperon, S. K. Pathak, M. B. Johnston, *et al.*, *Lead-free organic–inorganic tin halide perovskites for photovoltaic applications,* Energy & Environmental Science **7**, 3061 (2014).

[23] F. Hao, C. C. Stoumpos, D. H. Cao, R. P. Chang, and M. G. Kanatzidis, *Lead-free solid-state organic–inorganic halide perovskite solar cells,* Nature Photonics **8**, 489 (2014).

[24] T. Leijtens, R. Prasanna, A. Gold-Parker, M. F. Toney, and M. D. McGehee, *Mechanism of tin oxidation and stabilization by lead substitution in tin halide perovskites,* ACS Energy Letters **2**, 2159 (2017).

[25] W.-F. Yang, F. Igbari, Y.-H. Lou, Z.-K. Wang, and L.-S. Liao, *Tin halide perovskites: progress and challenges,* Advanced Energy Materials **10**, 1902584 (2020).

[26] T. Krishnamoorthy, H. Ding, C. Yan, W. L. Leong, T. Baikie, Z. Zhang, M. Sherburne, S. Li, M. Asta, N. Mathews, and S. G. Mhaisalkar, *Lead-free germanium iodide perovskite materials for photovoltaic applications,* Journal of Materials Chemistry A **3**, 23829 (2015).

[27] R. Chiara, M. Morana, and L. Malavasi, *Germanium-based halide perovskites: materials, properties, and applications,* ChemPlusChem **86**, 879 (2021).

[28] A. Raj, M. Kumar, H. Bherwani, A. Gupta, and A. Anshul, *Evidence of improved power conversion efficiency in lead-free CsGeI3 based perovskite solar cell heterostructure via scaps simulation,* Journal of Vacuum Science & Technology B **39**, (2021).

[29] C. C. Stoumpos, L. Frazer, D. J. Clark, Y. S. Kim, S. H. Rhim, A. J. Freeman, J. B. Ketterson, J. I. Jang, and M. G. Kanatzidis, *Hybrid germanium iodide perovskite semiconductors: active lone pairs, structural distortions, direct and indirect energy gaps, and strong nonlinear optical properties,* Journal of the American Chemical Society **137**, 6804 (2015).

[30] L. Tang, J. Y. Huang, C. Chang, M. Lee, and L. Liu, *New infrared nonlinear optical crystal CsGeBr3: synthesis, structure and powder second-harmonic generation properties,* Journal of Physics: Condensed Matter **17**, 7275 (2005).

[31] L. Chu, W. Ahmad, W. Liu, J. Yang, R. Zhang, Y. Sun, J. Yang, and X. Li, *Lead-free halide double perovskite materials: a new superstar toward green and stable optoelectronic applications,* Nano-Micro Letters **11**, 1 (2019).

[32] X.-G. Zhao, D. Yang, J.-C. Ren, Y. Sun, Z. Xiao, and L. Zhang, *Rational design of halide double perovskites for optoelectronic applications,* Joule **2**, 1662 (2018).

[33] F. Giustino and H. J. Snaith, *Toward lead-free perovskite solar cells,* ACS Energy Letters **1**, 1233 (2016).

[34] M. Wang, P. Zeng, S. Bai, J. Gu, F. Li, Z. Yang, and M. Liu, *High-quality sequential-vapor-deposited $Cs_2AgBiBr_6$ thin films for lead-free perovskite solar cells,* Solar RRL **2**, 1800217 (2018).

[35] E. Greul, M. L. Petrus, A. Binek, P. Docampo, and T. Bein, *Highly stable, phase pure $Cs_2AgBiBr_6$ double perovskite thin films for optoelectronic applications,* Journal of Materials Chemistry A **5**, 19972 (2017).

[36] J. Luo, X. Wang, S. Li, J. Liu, Y. Guo, G. Niu, L. Yao, Y. Fu, L. Gao, Q. Dong, C. Zhao, M. Leng, F. Ma, W. Liang, L. Wang, S. Jin, J. Han, L. Zhang, J. Etheridge, J. Wang, Y. Yan, E. H. Sargent, and J. Tang, *Efficient and stable emission of warm-white light from lead-free halide double perovskites,* Nature **563**, 541 (2018).

[37] L. Zhou, Y.-F. Xu, B.-X. Chen, D.-B. Kuang, and C.-Y. Su, *Synthesis and photocatalytic application of stable lead-free $Cs_2AgBiBr_6$ perovskite nanocrystals,* Small **14**, 1703762 (2018).

[38] W. Meng, X. Wang, Z. Xiao, J. Wang, D. B. Mitzi, and Y. Yan, *Parity-forbidden transitions and their impact on the optical absorption properties of lead-free metal*

halide perovskites and double perovskites, The Journal of Physical Chemistry Letters **8**, 2999 (2017).

[39] L.-Z. Lei, Z.-F. Shi, Y. Li, Z.-Z. Ma, F. Zhang, T.-T. Xu, Y.-T. Tian, D. Wu, X.-J. Li, and G.-T. Du, *High-efficiency and air-stable photodetectors based on lead-free double perovskite $Cs_2AgBiBr_6$ thin films,* Journal of Materials Chemistry C **6**, 7982 (2018).

[40] H. Li, X. Shan, J. N. Neu, T. Geske, M. Davis, P. Mao, K. Xiao, T. Siegrist, and Z. Yu, *Lead-free halide double perovskite-polymer composites for flexible X-ray imaging,* Journal of Materials Chemistry C **6**, 11961 (2018).

[41] F. Ji, G. Boschloo, F. Wang, and F. Gao, *Challenges and Progress in Lead-Free Halide Double Perovskite Solar Cells,* Solar RRL **7**, 2201112 (2023).

[42] E. T. McClure, M. R. Ball, W. Windl, and P. M. Woodward, *Cs2AgBiX6 (X= Br, Cl): new visible light absorbing, lead-free halide perovskite semiconductors,* Chemistry of Materials **28**, 1348 (2016).

[43] Y. Sun, A. J. Fernandez-Carrion, Y. Liu, C. Yin, X. Ming, B.-M. Liu, J. Wang, H. Fu, X. Kuang, and X. Xing, *Bismuth-based halide double perovskite Cs2LiBiCl6: crystal structure, luminescence, and stability,* Chemistry of Materials **33**, 5905 (2021).

[44] F. Ji, J. Klarbring, F. Wang, W. Ning, L. Wang, C. Yin, J. S. M. Figueroa, C. K. Christensen, M. Etter, T. Ederth, L. Sun, S. I. Simak, I. A. Abrikosov, and F. Gao, *Lead-Free Halide Double Perovskite $Cs_2AgBiBr_6$ with Decreased Band Gap,* Angewandte Chemie **132**, 15303 (2020).

[45] W. Tress and M. T. Sirtl, *$Cs_2AgBiBr_6$ double perovskites as lead-free alternatives for perovskite solar cells?,* Solar RRL **6**, 2100770 (2022).

[46] A. D. Wright, L. R. Buizza, K. J. Savill, G. Longo, H. J. Snaith, M. B. Johnston, and L. M. Herz, *Ultrafast excited-state localization in Cs2AgBiBr6 double perovskite,* The Journal of Physical Chemistry Letters **12**, 3352 (2021).

[47] F. Wei, Z. Deng, S. Sun, N. T. P. Hartono, H. L. Seng, T. Buonassisi, P. D. Bristowe, and A. K. Cheetham, *Enhanced visible light absorption for lead-free double perovskite $Cs_2AgSbBr_6$,* Chemical Communications **55**, 3721 (2019).

[48] Y. Liu, A. Nag, L. Manna, and Z. Xia, *Lead-free double perovskite $Cs_2AgInCl_6$,* Angewandte Chemie **133**, 11696 (2021).

[49] J. S. Bechtel and A. Van der Ven, *Octahedral tilting instabilities in inorganic halide perovskites,* Physical Review Materials **2**, 025401 (2018).

[50] J. Klarbring, O. Hellman, I. A. Abrikosov, and S. I. Simak, *Anharmonicity and ultralow thermal conductivity in lead-free halide double perovskites,* Physical Review Letters **125**, 045701 (2020).

[51] C. J. Howard and H. T. Stokes, *Group-theoretical analysis of octahedral tilting in perovskites,* Acta Crystallographica Section B: Structural Science **54**, 782 (1998).

[52] R. X. Yang, J. M. Skelton, E. L. Da Silva, J. M. Frost, and A. Walsh, *Spontaneous octahedral tilting in the cubic inorganic cesium halide perovskites CsSnX3 and CsPbX3 (X= F, Cl, Br, I),* The Journal of Physical Chemistry Letters **8**, 4720 (2017).

[53] V. M. Goldschmidt, *Die gesetze der krystallochemie,* Naturwissenschaften **14**, 477 (1926).

[54] A. M. Glazer, *The classification of tilted octahedra in perovskites,* Acta Crystallographica Section B: Structural Crystallography and Crystal Chemistry **28**, 3384 (1972).

[55] L. D. Landau and E. M. Lifshitz, *Statistical Physics: Volume 5* (Elsevier, 2013).

[56] S. Caicedo-Dávila, A. Cohen, S. G. Motti, M. Isobe, K. M. McCall, M. Grumet, M. V. Kovalenko, O. Yaffe, L. M. Herz, D. H. Fabini, *et al.*, *Disentangling the effects of structure and lone-pair electrons in the lattice dynamics of halide perovskites,* Nature Communications **15**, 4184 (2024).

[57] J. Wiktor, U. Rothlisberger, and A. Pasquarello, *Predictive determination of band gaps of inorganic halide perovskites,* The Journal of Physical Chemistry Letters **8**, 5507 (2017).

[58] X.-G. Zhao, G. M. Dalpian, Z. Wang, and A. Zunger, *Polymorphous nature of cubic halide perovskites,* Physical Review B **101**, 155137 (2020).

[59] G.-W. Kim and A. Petrozza, *Defect tolerance and intolerance in metal-halide perovskites,* Advanced Energy Materials **10**, 2001959 (2020).

[60] I. Levine, O. G. Vera, M. Kulbak, D.-R. Ceratti, C. Rehermann, J. A. Márquez, S. Levcenko, T. Unold, G. Hodes, I. Balberg, D. Cahen, and T. Dittrich, *Deep defect states in wide-band-gap ABX_3 halide perovskites,* ACS Energy Letters **4**, 1150 (2019).

[61] A. S. Alexandrov, *Polarons in advanced materials* (Springer Science & Business Media, 2008).

[62] C. Franchini, M. Reticcioli, M. Setvin, and U. Diebold, *Polarons in materials,* Nature Reviews Materials **6**, 560 (2021).

[63] X.-Y. Zhu and V. Podzorov, *Charge carriers in hybrid organic–inorganic lead halide perovskites might be protected as large polarons,* 2015.

[64] F. Zheng and L.-w. Wang, *Large polaron formation and its effect on electron transport in hybrid perovskites,* Energy & Environmental Science **12**, 1219 (2019).

[65] D. Ghosh, E. Welch, A. J. Neukirch, A. Zakhidov, and S. Tretiak, *Polarons in halide perovskites: a perspective,* The Journal of Physical Chemistry Letters **11**, 3271 (2020).

[66] M. Baskurt and J. Wiktor, *Charge Localization in $Cs_2AgBiBr_6$ Double Perovskite: Small Polarons and Self-Trapped Excitons,* The Journal of Physical Chemistry C **127**, 23966 (2023).

[67] R. Williams and K. Song, *The self-trapped exciton,* Journal of Physics and Chemistry of Solids **51**, 679 (1990).

[68] J. Li, H. Wang, and D. Li, *Self-trapped excitons in two-dimensional perovskites,* Frontiers of Optoelectronics **13**, 225 (2020).

[69] J. Yu, J. Kong, W. Hao, X. Guo, H. He, W. R. Leow, Z. Liu, P. Cai, G. Qian, S. Li, X. Chen, and X. Chen, *Broadband extrinsic self-trapped exciton emission in Sn-doped 2D lead-halide perovskites,* Advanced Materials **31**, 1806385 (2019).

[70] L. Zhou, J.-F. Liao, Z.-G. Huang, J.-H. Wei, X.-D. Wang, H.-Y. Chen, and D.-B. Kuang, *Intrinsic self-trapped emission in 0D lead-free $(C_4H_{14}N_2)_2In_2Br_{10}$ single crystal,* Angewandte Chemie **131**, 15581 (2019).

[71] M. D. Smith and H. I. Karunadasa, *White-light emission from layered halide perovskites,* Accounts of Chemical Research **51**, 619 (2018).

[72] E. R. Dohner, A. Jaffe, L. R. Bradshaw, and H. I. Karunadasa, *Intrinsic white-light emission from layered hybrid perovskites,* Journal of the American Chemical Society **136**, 13154 (2014).

[73] T. Hu, M. D. Smith, E. R. Dohner, M.-J. Sher, X. Wu, M. T. Trinh, A. Fisher, J. Corbett, X.-Y. Zhu, H. I. Karunadasa, and A. M. Lindenberg, *Mechanism for broadband white-light emission from two-dimensional (110) hybrid perovskites,* The Journal of Physical Chemistry Letters **7**, 2258 (2016).

[74] M. D. Smith, B. A. Connor, and H. I. Karunadasa, *Tuning the luminescence of layered halide perovskites,* Chemical Reviews **119**, 3104 (2019).

[75] D. M. Ceperley and B. J. Alder, *Ground state of the electron gas by a stochastic method,* Physical Review Letters **45**, 566 (1980).

[76] J. P. Perdew, K. Burke, and M. Ernzerhof, *Generalized gradient approximation made simple,* Physical Review Letters **77**, 3865 (1996).

[77] J. P. Perdew and W. Yue, *Accurate and simple density functional for the electronic exchange energy: Generalized gradient approximation,* Physical Review B **33**, 8800 (1986).

[78] J. P. Perdew, A. Ruzsinszky, G. I. Csonka, O. A. Vydrov, G. E. Scuseria, L. A. Constantin, X. Zhou, and K. Burke, *Restoring the density-gradient expansion for exchange in solids and surfaces,* Physical Review Letters **100**, 136406 (2008).

[79] P. Mori-Sánchez, A. J. Cohen, and W. Yang, *Localization and delocalization errors in density functional theory and implications for band-gap prediction,* Physical Review Letters **100**, 146401 (2008).

[80] A. J. Cohen, P. Mori-Sánchez, and W. Yang, *Fractional charge perspective on the band gap in density-functional theory,* Physical Review B **77**, 115123 (2008).

[81] A. D. Becke, *A new mixing of Hartree–Fock and local density-functional theories,* The Journal of Chemical Physics **98**, 1372 (1993).

[82] J. P. Perdew, M. Ernzerhof, and K. Burke, *Rationale for mixing exact exchange with density functional approximations,* The Journal of Chemical Physics **105**, 9982 (1996).

[83] M. Ernzerhof and G. E. Scuseria, *Assessment of the Perdew–Burke–Ernzerhof exchange-correlation functional,* The Journal of Chemical Physics **110**, 5029 (1999).

[84] C. Adamo and V. Barone, *Toward reliable density functional methods without adjustable parameters: The PBE0 model,* The Journal of Chemical Physics **110**, 6158 (1999).

[85] T. Bischoff, I. Reshetnyak, and A. Pasquarello, *Adjustable potential probes for band-gap predictions of extended systems through nonempirical hybrid functionals,* Physical Review B **99**, 201114 (2019).

[86] K. Sharkas, K. Wagle, B. Santra, S. Akter, R. R. Zope, T. Baruah, K. A. Jackson, J. P. Perdew, and J. E. Peralta, *Self-interaction error overbinds water clusters but cancels in structural energy differences,* Proceedings of the National Academy of Sciences **117**, 11283 (2020).

[87] J. P. Perdew, R. G. Parr, M. Levy, and J. L. Balduz Jr, *Density-functional theory for fractional particle number: derivative discontinuities of the energy,* Physical Review Letters **49**, 1691 (1982).

[88] H. J. Berendsen, J. v. Postma, W. F. Van Gunsteren, A. DiNola, and J. R. Haak, *Molecular dynamics with coupling to an external bath,* The Journal of Chemical Physics **81**, 3684 (1984).

[89] R. L. Davidchack, R. Handel, and M. V. Tretyakov, *Langevin thermostat for rigid body dynamics,* The Journal of Chemical Physics **130**, 234101 (2009). doi:10.1063/1.3149788.

[90] S. Nosé, *A unified formulation of the constant temperature molecular dynamics methods,* The Journal of Chemical Physics **81**, 511 (1984).

[91] W. G. Hoover, *Canonical dynamics: Equilibrium phase-space distributions,* Physical Review A **31**, 1695 (1985).

[92] M. Bernetti and G. Bussi, *Pressure control using stochastic cell rescaling,* The Journal of Chemical Physics **153**, (2020).

[93] W. S. McCulloch and W. Pitts, *A logical calculus of the ideas immanent in nervous activity,* The Bulletin of Mathematical Biophysics **5**, 115 (1943).

[94] Z. Fan, Z. Zeng, C. Zhang, Y. Wang, K. Song, H. Dong, Y. Chen, and T. Ala-Nissila, *Neuroevolution machine learning potentials: Combining high accuracy and low cost in atomistic simulations and application to heat transport,* Physical Review B **104**, 104309 (2021).

[95] Z. Fan, *Improving the accuracy of the neuroevolution machine learning potential for multi-component systems,* Journal of Physics: Condensed Matter **34**, 125902 (2022).

[96] L. Breiman, *Bagging predictors,* Machine Learning **24**, 123 (1996).